AD-A159 682 INVESTIGATION OF THE SPATIALLY ISOTROPIC COMPONENT OF THE LATERALLY AVERA..(U) CHICAGO UNIV IL JAMES FRANCK INST C F YU ET AL. AUG 85 TR-6 N00014-77-C-0240 1/1

UNCLASSIFIED F/G 20/10 NL

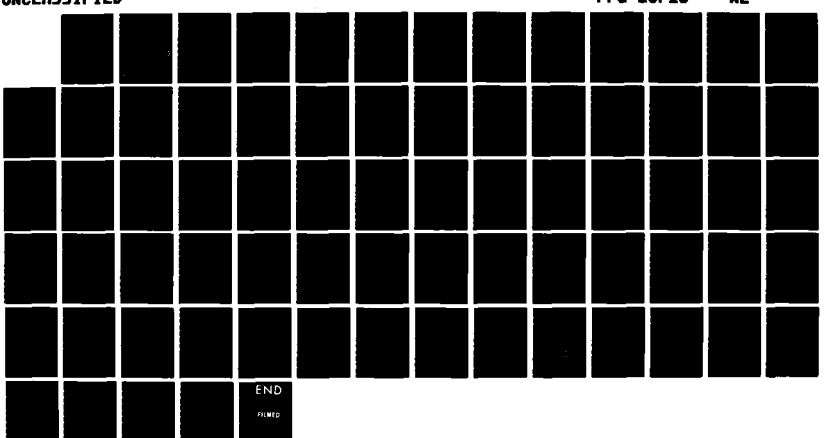

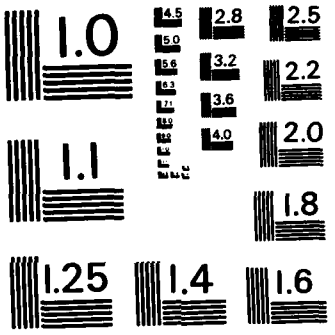

unclassified

SECURITY CLASSIFICATION OF THIS PAGE (When Data Entered)

(2)

REPORT DOCUMENTATION PAGE		READ INSTRUCTIONS BEFORE COMPLETING FORM
1. REPORT NUMBER 6	2. GOVT ACCESSION NO.	3. RECIPIENT'S CATALOG NUMBER
4. TITLE (and Subtitle) INVESTIGATION OF THE SPATIALLY ISOTROPIC COMPONENT OF THE LATERALLY AVERAGED MOLECULAR HYDROGEN/Ag(111) PHYSISORPTION POTENTIAL		5. TYPE OF REPORT & PERIOD COVERED Interim Technical Report 6. PERFORMING ORG. REPORT NUMBER
7. AUTHOR(s) Chien-fan Yu, K. Birgitta Whaley, C. S. Hogg and Steven J. Sibener		8. CONTRACT OR GRANT NUMBER(s) N00014-77-C-0240
9. PERFORMING ORGANIZATION NAME AND ADDRESS The University of Chicago The James Franck Institute 5640 South Ellis Avenue, Chicago, IL 60637		10. PROGRAM ELEMENT, PROJECT, TASK AREA & WORK UNIT NUMBERS NR-392-023
11. CONTROLLING OFFICE NAME AND ADDRESS The Office of Naval Research Physical Sciences Division (Code 421) 800 North Quincy Str., Arlington, VA 22217		12. REPORT DATE August 1985 13. NUMBER OF PAGES 70
14. MONITORING AGENCY NAME & ADDRESS(if different from Controlling Office)		15. SECURITY CLASS. (of this report) unclassified 15a. DECLASSIFICATION/DOWNGRADING SCHEDULE

16. DISTRIBUTION STATEMENT (of this Report)

This document has been approved for public release and sale; its distribution is unlimited.

17. DISTRIBUTION STATEMENT (of the abstract entered in Block 20, if different from Report)

18. SUPPLEMENTARY NOTES

Prepared for Publication in Journal of Chemical Physics

Cont'd

19. KEY WORDS (Continue on reverse side if necessary and identify by block number)

Gas-surface interaction potentials; physisorption; selective adsorption; para-hydrogen generation; gas-surface scattering resonances.

20. ABSTRACT (Continue on reverse side if necessary and identify by block number)

A comprehensive study of the spatially isotropic component of the laterally averaged molecular hydrogen/Ag(111) physisorption potential is presented. Diffractive selective adsorption scattering resonances for rotationally state-selected H_2 and D_2 on Ag(111) have been mapped out as a function of incident polar angle for several crystal azimuths and beam energies. These resonances have been used to determine the bound eigenvalues, and subsequently the shape, of the potential well. Best fit Lennard-Jones, Morse, variable exponent, and exponential-3 potentials having well depths ~32 meV are derived from the data. These measure-

DD FORM 1 JAN 73 1473 EDITION OF 1 NOV 68 IS OBSOLETE
S/N 0102-LF-014-6601

unclassified
SECURITY CLASSIFICATION OF THIS PAGE (When Data Entered)

ments are supported by rotationally inelastic scattering measurements for HD and exact close-coupled quantum scattering calculations. Debye-Waller attenuation measurements are also presented for H_2, D_2, and HD. The ability to detect these diffractively coupled resonances on a closest-packed metallic surface, i.e. a surface of extremely low corrugation, suggests that such measurements can be carried out on a much wider class of surfaces than previously envisioned.

A COMPLETE COPY OF THE MANUSCRIPT WILL BE SENT UPON REQUEST.

INVESTIGATION OF THE SPATIALLY ISOTROPIC COMPONENT OF THE LATERALLY AVERAGED MOLECULAR HYDROGEN/Ag(111) PHYSISORPTION POTENTIAL

Chien-fan Yu[(a)], K. Birgitta Whaley[(b)], C. S. Hogg and Steven J. Sibener[†]

Department of Chemistry and
The James Franck Institute
The University of Chicago
5640 South Ellis Avenue
Chicago, Illinois 60637

In Press, Journal of Chemical Physics

[†]Alfred P. Sloan Fellow
PACS: 79.20.Rf

(a) Current Address: Dept. of Chemistry, Columbia University, New York

(b) Current Address: Dept. of Chemistry, Tel Aviv University, Israel

ABSTRACT

A comprehensive study of the spatially isotropic component of the laterally averaged molecular hydrogen/Ag(111) physisorption potential is presented. Diffractive selective adsorption scattering resonances for rotationally state-selected H_2^{η} and D_2^{η} on Ag(111) have been mapped out as a function of incident polar angle for several crystal azimuths and beam energies. These resonances have been used to determine the bound eigenvalues, and subsequently the shape, of the potential well. Best fit Lennard-Jones, Morse, variable exponent, and exponential-3 potentials having well depths of ~32 meV are derived from the data. These measurements are supported by rotationally inelastic scattering measurements for HD and exact close-coupled quantum scattering calculations. Debye-Waller attenuation measurements are also presented for H_2^{η}, D_2^{η}, and HD. The ability to detect these diffractively coupled resonances on a closest-packed metallic surface, i.e. a surface of extremely low corrugation, suggests that such measurements can be carried out on a much wider class of surfaces than previously envisioned.

Originator Supplied Keywords include:

Introduction

There is currently great interest in formulating an accurate description of gas-surface interaction potentials for a wide variety of systems. This is clearly indicated by the large body of recent experimental and theoretical work in this area [1, 2]. The motivation for these studies is rather straightforward: knowledge of the interaction potential is a prerequisite for a complete understanding of many important heterogeneous processes such as oxidation, catalysis, condensation, and energy transfer, and is intimately related to the structure, charge density distribution, and dynamics of the surface. The central theme of this paper will be to present a detailed study of the spatially isotropic component of the laterally averaged molecular hydrogen/Ag(111) physisorption potential. This will be accomplished, in part, by using diffractive selective adsorption (DSA) scattering resonances to determine the bound eigenvalues of the potential. Resonances of this type were first observed by Estermann and Stern in 1930 [3], and subsequently explained by Lennard-Jones and Devonshire [4]. This phenomenon, due to both the excellent energy resolution of contemporary gas-surface scattering instruments and the implementation of accurate quantum scattering calculations, provides the most valuable means of determining laterally averaged physisorption potentials at this time.

For the physisorption interaction of atoms and molecules with surfaces of perfect periodicity, the interaction potential with a stationary lattice can be expanded as a Fourier sum over the surface reciprocal lattice vectors, $\underset{\sim}{G}$. For atom-surface systems

$$V(z, \underset{\sim}{R}) = \sum_{\underset{\sim}{G}} V_{\underset{\sim}{G}}(z)\, e^{i\underset{\sim}{G}\cdot\underset{\sim}{R}} \qquad (1.1)$$

with z the perpendicular distance of the atom from the surface and $\underset{\sim}{R}$ the surface projection of its distance from some origin of coordinates located in the surface (xy) plane. In the molecular case, eg. for a diatomic molecule, $V_{\underset{\sim}{G}}(z)$ is replaced

by $V_G(z, \theta, \phi, r)$ where θ, ϕ, and r are the additional spherical polar internal coordinates of the diatom and z, $\underset{\sim}{R}$ now refer to the location of the molecule center of mass in the surface fixed coordinate system. Neglecting in the first approximation the internal degrees of freedom for the molecular case, the laterally averaged interaction potential $V_{00}(z)$ can be divided into two components: an attractive long range polarization potential, $V_{00,A}(z)$ and a short range repulsive potential, $V_{00,R}(z)$. The asymptotic form of the van der Waals term is well established as [5, 6]

$$V_{00,A}(z) \sim -C_3/(z-z_0)^3 \qquad (1.2)$$

where z is the normal distance between the adparticle center of mass and the surface. Both C_3 and the position of the reference plane, z_0, have been calculated for a number of atom-solid systems [6]. Ab initio calculation of the repulsive component requires knowledge of both the electronic structure of the surface and the adparticle, and inclusion of both Coulombic and exchange terms. Several calculations have been made for the interaction of helium with jellium surfaces [7]. Recently Harris and Liebsch [8] have calculated a repulsive potential for He/Cu(110) containing two adjustable parameters which gives good agreement with the available scattering data on this system [9]. Since their approach applies to any adparticle with a closed shell electronic structure, it was also possible to provide an estimate of the corresponding H_2/Cu(110) potential [10], including an estimate of the anisotropic contribution to the laterally averaged physisorption potential $V_{00}(z, \theta, \phi, r)$. Such ab initio calculations on real systems present considerable difficulties. In this respect, a recent suggestion that the repulsive He-surface interaction potential can be approximated as a local function of the surface electronic charge density [11] may indicate a viable practical alternative approach to the ab initio calculation of other physisorption potentials [12].

By comparison, the approach we take here is the empirical determination of the

laterally averaged potential which is the result of extensive molecule-surface scattering experiments and theoretical scattering calculations. Molecular and atomic beam scattering experiments allow determination of the physisorption well depth D, the bound states of the laterally averaged potential (and, therefore, the shape of the well), but not its absolute position with respect to the surface atoms. In addition, molecular scattering gives information on the anisotropic (i.e. orientation dependent) component of the laterally averaged potential. Extensive experiments and calculations on scattering of the hydrogen isotopes H_2, D_2, and HD from Ag(111) have allowed us to make a detailed analysis of the full laterally averaged physisorption potential on this closely packed and extremely smooth surface. In this paper we present the results relating to the spatially isotropic component of the molecular hydrogen/Ag(111) potential. The anisotropic component will be presented in a forthcoming paper [13].

In these experiments we measure both diffractive selective adsorption, DSA, and rotationally mediated selective adsorption, RMSA, resonances for H_2 and D_2 on Ag(111). This is one of the first studies reported in which DSA techniques have been successfully used on a closest packed (i.e., extremely low corrugation) metallic surface to extract information on a physisorption potential, and demonstrates, together with data on the hydrogen/Pt(111) system [14], that such measurements can be carried out on a much wider class of surfaces than previously thought possible. Experiments in this field have focussed primarily on studies of DSA resonances in the scattering of light particles (He, H and H_2) from highly corrugated surfaces of dielectrics like LiF [15], NaF [16], graphite [17-19], and stepped metal surfaces of copper [9]. The scarcity of DSA results on metals may be attributed to the very low non-zero order diffraction probabilities resulting from the small corrugation of metal surfaces [20]. However, the observation that H_2 diffraction peaks on Ag(111) are an order of magnitude stronger than He peaks [21] under equivalent incident conditions suggests that H_2 scattering from Ag(111) is a promising

candidate for molecular DSA studies. This observation was explained by Hill et al. [22] in terms of a lateral variation of the van der Waals interaction, and more recently by Liebsch and Harris [23] in terms of differences in the repulsive component of the interaction. Silver is a good substrate for DSA experiments since it is chemically inert with respect to hydrogen chemisorption, so the beam scattering experiments can be done at surface temperatures down to ~30 K without interference due to hydrogen loading of the surface. The use of low surface temperatures together with molecular beams of very low energy minimizes Debye-Waller type attenuation, and enables us to overcome the difficulty of detecting resonances coupled via very low diffraction probabilities. Low corrugation actually facilitates the analysis of DSA experiments since it virtually eliminates any complications due to band structure [24].

Past DSA studies on molecular hydrogen have treated it as a structureless particle [18]. However, it is to be expected that bound state energy levels obtained from selective adsorption measurements will be affected by the spatially anisotropic component of the molecule-surface interaction potential. Recent low energy electron energy loss (EELS) experiments on the physisorption of H_2 and D_2 on Ag(111) [25] and of H_2, D_2 and HD on Cu(110) [26] indicate that molecular hydrogen behaves as a nearly free 3-dimensional rotor on these surfaces. However, the resolution was too low (12 meV for Ag(111), 3 meV for Cu(100)) for quantitative measurement of any deviation from the unhindered results. In EELS experiments the spatial anisotropy should manifest itself in slight shifts of the observed vibration-rotation transitions for physisorbed $|J,m\rangle$ states, and as a consequence of this, in linewidth changes for spectra obtained as a convolution over various m sub-states. Calculations on the RMSA resonances of HD on Pt(111) and HD on Ag(111) have shown that RMSA resonances of physisorbed HD are consistent with bound states of the isotropic component plus a first order level shift deriving from the anisotropic component of the interaction potential [27, 28].

The inadequacy of a free rotor approximation is also evidenced in other calculations for the HD/Pt(111) system [29]. This shift in general will be J and m dependent. Similar |J,m> dependent shifts should also appear in the bound state spectrum of the physisorption well when probed by selective adsorption scattering resonances. Comparison of DSA resonance energies for n-H_2 (J = 1: J = 0 is 3:1) and p-H_2 and both DSA and RMSA resonances for n-D_2 (J = 1: J = 0 is 1:2) and o-D_2 have enabled us to directly detect an m state averaged shift in these experiments.

The plan for the remainder of the paper is as follows: Sections 2, 3 and 4 describe the apparatus, construction of the p-H_2 and o-D_2 converter, and the experimental procedure. Section 5 describes the Debye-Waller analysis and problems arising from this for the molecular case. The kinematics of selective adsorption resonances are analyzed in detail in Section 6 and the connection between DSA and RMSA is given explicitly. The experimental selective adsorption data are presented in Section 7 and quantum number assignments discussed in Section 8. The isotopic study of p-H_2 and o-D_2 (J = 0) resonances according to the semiclassical method of Le Roy [30] gives two possible quantum number assignments: we distinguished between these by performing rotationally inelastic quantum scattering calculations for HD on Ag(111) for model potentials derived from each assignment, and comparing the results to experimental HD rotationally inelastic transition probabilities. Section 9 contains a brief comparison with a recently proposed scaling relation of Vidali et al. [31], which further distinguishes the two quantum assignments. Thermal desorption experiments are described in Section 10. Finally, Section 11 presents a brief summary and our conclusions.

II. Apparatus

The scattering apparatus used in these experiments has been previously described [28, 32]. It consists of four major sections: the beam source and vacuum manifold, rotating detector, crystal assembly and associated surface analysis instrumentation, and data acquisition electronics.

The nozzle beam is differentially pumped in three stages in a non-bakeable source chamber, with typical operating pressure being 5×10^{-3}, 1×10^{-5}, and 5×10^{-7} torr for the regions before the skimmer, before the beam collimator, and containing the chopper, respectively. The main UHV scattering chamber is separated from the three source chamber regions by a bakeable buffer region whose pressure rises to 5×10^{-9} torr when the beam is on. This buffer section is separated from the chopper section by a sliding gate valve which contains the 0.5 mm diam. beam defining aperature. Supported by a 400 1/s ion pump and a titanium sublimation pump, the crystal chamber has a base pressure of 7×10^{-11} torr, which rises as high as 1×10^{-9} torr when the beam is on. The incident beam is collimated to an angular divergence of 0.1^{o}, which corresponds to a 0.5mm diam. beam spot at the crystal.

Particle detection is accomplished with a doubly differentially pumped quadrupole mass spectrometer, which rotates about a horizontal axis in the plane containing the incident beam and the surface normal. The electron bombardment ionizer is located 14.45 cm from the sample, and is collimated to view the crystal with 0.67^{o} resolution. The detector can be rotated manually or under computer control.

The crystal manipulator provides x, y, and z translational degrees of freedom, incident polar angle and surface azimuthal angle scanning, and in-plane and out-of-plane tilt adjustment. The retractable CMA Auger spectrometer with a side mounted ion-sputtering gun can be placed under or away from the sample before and after ion sputtering or taking Auger spectra.

Data acquisition and instrument control is carried out with a PDP-11 minicomputer which is interfaced to the scattering apparatus via CAMAC. Time-of-flight measurements are made with a 255 channel scaler which has a minimum dwell time of 0.25μsec/channel. Molecular beam gating is carried out with a 15.24 cm diam. chopper which contains two narrow slots for velocity analysis (0.5mm wide) and two 50% duty cycle patterns for angular distribution measurements. Angular distributions are obtained with two 32 bit scalers which are synchronized to the chopper in order to collect signal plus background (slot open) and background only (slot closed) information. DSA signals were collected by a Keithley electrometer, demodulated by a lock-in amplifier, passed to a digital voltmeter, and finally read into the computer.

III. $p\text{-}H_2$ and $o\text{-}D_2$ Generation

The molecular nuclear state degeneracies of H_2 and D_2 give rise to the para/ortho population ratio of 1:3 for H_2 (normal-H_2) and 1:2 for D_2 (normal-D_2) in the high temperature limit. These ratios will not change in the course of supersonic jet expansion. For an ideal expansion the terminal rotational state distribution of H_2 will be 25% J = 0 state ($p\text{-}H_2$) and 75% J = 1 state ($o\text{-}H_2$). Similarly the D_2 beam will be 33% J = 1 ($p\text{-}D_2$) and about 67% J = 0 ($o\text{-}D_2$). In order to prepare pure rotational ground state beams of H_2 and D_2, conversion to $p\text{-}H_2$ and $o\text{-}D_2$ has to be made before the jet expansion.

An in-line p-hydrogen/o-deuterium converter was constructed as shown in Figure 1. The converter consists of a coaxial stainless steel tube arrangement which contains a nickel salt-based catalyst, APPACHI [33], in its outer tube. A sintered stainless steel filter element was welded to the end of the inner tube to prevent the catalyst from entering this region of the converter. The catalyst was activated by heating at 150 to 175^{0} C for a few hours while flowing a small stream of hydrogen gas through it [34]. In operation, the converter was immersed

in a liquid hydrogen dewar to maintain a very low temperature, ensuring excellent conversion to J = 0 hydrogen.

When n-H_2 or n-D_2 are brought into the converter, exposure to the strong magnetic field gradients at the surface of the catalyst will quickly promote equilibration at this low temperature, i.e. 99.8% p-H_2 and 97.8 o-D_2. The almost pure p-H_2 or o-D_2 then exits through the inner tube to the nozzle. The converter can operature at pressures up to 2000 psig, more than that required for producing for a good jet expansion. A by-pass line was also incorporated to facilitate immediate switching between n-/p-H_2 or n-/o-D_2.

Comparison of the rotationally inelastic scattering transition probabilities for H_2 or D_2 with and without conversion can be used to check the effectiveness of the converter. Figures 2 and 3 show the angular distributions of H_2 and D_2 scattering from Ag(111) with or without conversion. By subtracting the diffuse background and deconvoluting the instrumental factors from the specular and inelastic peaks, relative probabilities of the J = 0 → 2 transition to that of the specular beam can be obtained, and are listed in the last column of Table 1.

The rotational state populations in the expanded jet can be estimated by solving the energy balance equation [35]:

$$\frac{5}{2} k_B T_o + E_r(T_o) = \frac{1}{2} M u^2 + \frac{5}{2} k_B T_p + E_r(T_r) \qquad (3.1)$$

where T_o is the source temperature, u the stream velocity, T_p parallel temperature of the beam, and T_r the rotational temperature of the beam. A Boltzmann distribution of rotational states is assumed in the non-commuting isothermal canonical ensembles of para and ortho components. The results are also shown in Table 1. It is clear that the population of the J = 0 H_2 increases by a factor of four after conversion which is close to the ratio of the relative probability of the J = 0 → 2 transition of p-H_2 to that of n-H_2. Similarly, the J = 0 D_2 increases by a factor of 1.5 which is approximately the ratio of the relative probability of

fall on three sets of concentric arcs centered around $\underset{\sim}{G} = (\bar{1}0)$, $(0\bar{1})$, and $(\bar{1}\bar{1})$. Bound state energies for J = 0 H_2 can be directly calculated from arcs using Eq. (6.7) to analyze the data. Similar measurements have also been made using o-D_2, as shown in Figures 13 and 14. In addition to the o-D_2 DSA dips, two RMSA dips also appear (dash-dot-dot lines) as broader, azimuth-independent features, for which bound state energies $\varepsilon_{n,Jo}$ can be calculated using Eq. (6.15). Another observation is that no discernible splittings occur at $\phi = 30^o$ between the resonances coupled by the (11) and (10) lattice points, i.e. the two groups of arcs coalesce smoothly at this azimuth. This absence of band structure at the crossing points of the arcs is presumably due to the very small non-zero order Fourier components of the periodic surface potential [24].

Figures 15 and 16 show the specular intensity spectra for n-H_2 and n-D_2, respectively, taken at three different beam energies along the $<11\bar{2}>$ direction. The resonances can be seen to get stronger and broader as the beam energy is lowered. These energy dependent runs serve to confirm our level assignments, and demonstrate that low energy DSA spectra are more sensitive, and have better energy resolution, than higher energy experiments. The low energy data has in fact enabled detection of an extra bound state near the top of the well for both H_2 and D_2. The estimated accuracy of the bound state resonance energies determined with the low energy incident beam are ca. 0.2 meV for H_2 and 0.15 meV for D_2. The selective adsorption loci for both isotopes have also been mapped out in the K_x-K_y reciprocal lattice plane at beam energies of approximately 35 and 80 meV, yielding results in agreement with the low energy data. The higher energy H_2 spectra contain resonance dips due to an additional bound state, $\varepsilon_o \approx -25.7$ meV.

were achieved by redesigning the cryogenic connections to the crystal mount, thereby decreasing Debye-Waller attenuation of the specular beam. The crystal mount was also modified to include a pointer and vernier scale which allowed the azimuthal angle to be accurately set for orientations falling between the $\langle 11\bar{2} \rangle$ and $\langle 10\bar{1} \rangle$ symmetry directions (see Section IV). In addition, a new beam source was constructed in which the nozzle assembly was directly mounted on a liquid cryogen reservoir located in the nozzle-skimmer vacuum region. This allowed us to produce an extremely stable H_2 beam of lower energy than was previously available in our laboratory. The actual beam pumping manifold was also rebuilt, eliminating booster pumps in the nozzle-skimmer region, and replacing them with high throughput diffusion pumps. This last modification resulted in the production of more intense hydrogen beams of narrower velocity dispersion. Finally, in order to address concerns pertaining to the then unknown magnitude of the resonance energy shifts occurring due to the $J \neq 0$ components in the incident beam, an in-line $p\text{-}H_2/o\text{-}D_2$ converter was designed and fabricated (Section III).

Figure 11 displays eight $p\text{-}H_2$ resonance spectra taken at successive azimuthal angles. DSA dips appearing in these runs are linked by distinguishable lines which group the resonances according to the pertinent coupling reciprocal lattice vector (mn). Individual dips are designated by $\left(\begin{smallmatrix}\nu \\ mn\end{smallmatrix}\right)$, where ν is the quantum number of the level. (The manner in which these assignments are made will be discussed in detail in Section VIII.) The positions of the dips attributable to a given coupling $\underset{\sim}{G}$ vector clearly shift in a similar manner as the crystal azimuth is varied. This feature is readily seen in Figure 12, which is the corresponding plot for the DSA resonances presented in the surface reciprocal lattice $K_x\text{-}K_y$ plane. The resonance dip positions, represented by points in this figure, clearly

$$V_{oo}(z, \theta) = v^{o}_{oo}(z) + v^{2}_{oo}(z)\ P_2(\cos\theta) \tag{6.21}$$

and

$$\varepsilon^{(1)}_{n,Jm} = \langle n|v^{2}_{oo}(z)|n\rangle\langle Jm|P_2(\cos\theta)|Jm\rangle \tag{6.22}$$

Even though the strength of the anisotropic term $v^{2}_{oo}(z)$ is very weak for H_2 and D_2, the effects of these shifts are large enough to be observed by comparison of the resonance positions and widths for normal H_2 ($J = 1 : J = 0$ is 3:1) and normal D_2 ($J = 1 : J = 0$ is 1:2) with those of para-H_2 and ortho-D_2 respectively. A preliminary report of these shifts has already appeared [51]. In addition, since for $J = J_i = 0$ ($m = m_i = 0$) $\varepsilon^{(1)}_{n,Jm}$ is zero, comparison of the DSA resonance energy with the RMSA resonance energy from the same level n when $J_i = 0$ provides a sensitive means of isolating the effect of the anisotropic component $v^{2}_{oo}(z)$, provided the isotropic component $v^{o}_{oo}(z)$ is known. This will be discussed in detail in a forthcoming paper [13]. We now present the selective adsorption results for normal and state selected ($J = 0$) H_2 and D_2.

VII. Selective Adsorption Resonances: Experimental Results

During the early stages of this work only n-H_2 and n-D_2 were available for use in searching for the presence of DSA resonances on Ag(111). The existence of discernible DSA dips was first confirmed by comparing specular intensity data, taken as a function of incident polar angle, at azimuthal angles *symmetric* about the $\langle 11\bar{2}\rangle$ direction, as shown in Figure 10 for $\phi = \pm 20^{o}$. In this figure weak but distinctive pairs of dips can be seen in the $\phi = 20^{o}$ and $\phi = -20^{o}$ spectra, as indicated by the six dashed lines. The presence of these low signal-to-noise features in both spectra, as required by the symmetry of the reciprocal lattice with respect to the $\langle 11\bar{2}\rangle$ direction, provided us with the necessary motivation to map out these resonances across the K_x-K_y plane.

Several instrumental improvements were then made with the intent of increasing the quality and precision of the data. Colder surface temperatures

$$= \varepsilon_{n,Jm}^{(0)} + \varepsilon_{n,Jm}^{(1)} + \frac{\hbar^2}{2M} (\underset{\sim}{K}_i + \underset{\sim}{G})^2 \qquad (6.19)$$

For the rotationally elastic case, $J = J_i$, this reduces to pure DSA, with resonance condition

$$\frac{\hbar^2 k_i^2}{2M} = \varepsilon_n^{(0)} + \varepsilon_{n,Jm}^{(1)} + \frac{\hbar^2}{2M} (\underset{\sim}{K}_i + \underset{\sim}{G})^2 \qquad (6.20)$$

and we see that the DSA resonance energies also show first order shifts $\varepsilon_{n,Jm}^{(1)}$.

An important distinction between pure DSA and pure RMSA resonances is that the former are azimuthally dependent, Eq. (6.20), while the later show no azimuthal dependence, Eqs. (6.14-15). Mixed DSA-RMSA resonances will also be azimuthally dependent, Eqs. (6.18-19). No evidence for such azimuthally dependent resonances have been observed to date in HD (specular) rotationally inelastic scattering from surfaces. The relative magnitude of the rotational coupling on smooth metal surfaces is so much greater than diffractive coupling for HD, that the small azimuthally dependent variations in the specular beam rotational distributions due to diffractive coupling are not detectable at the present sensitivity.

However, the situation is very different for the homonuclear hydrogen isotopes. Although again no mixed DSA-RMSA resonances have been observed yet, the very much smaller rotational inelasticity makes rotational and diffraction excitation probabilities of comparable magnitude and we find resonances in the specular beam which fall into two groups. These are i) azimuthally dependent resonances, due to DSA (Eq. 6.20) and ii) azimuthally independent resonances, due to pure RMSA (Eqs. (6.14, 6.15)). The first order level shift in these resonance conditions thus implies a dependence on the J and m quantum numbers of the initial state for DSA resonance energies, and a dependence on J and m of both the initial state and the closed rotational channel coupled to this at the resonance for RMSA. For H_2 and D_2 the laterally averaged potential may be represented by the first two symmetric terms in a Legendre expansion

where $v_{oo}^{o}(z)$ is the spatially isotropic component which is the same for all isotopes (H_2, D_2, and HD). The first order approximation to the rotational resonance energies is then given by eigenvalues of the rotationally decoupled equations

$$[\frac{d^2}{dz^2} + k_z^2 + \frac{M}{I} J_i(J_i + 1) - \frac{M}{I} J(J + 1) - \frac{2M}{\hbar^2} v_{oo}^{o}(z)]\chi_{Jm}(z) = \sum_{\ell = 0,1,\ldots} \frac{2M}{\hbar^2} \tilde{v}_{oo}^{\ell}(z) \langle Jm|P_\ell(\cos\theta)|Jm\rangle \chi_{Jm}(z) \tag{6.13}$$

For the homonuclear isotopes, $\tilde{v}_{oo}(z)$ is equal to zero [13]. Provided $v_{oo}^{o}(z)$ is greater than $\tilde{v}_{oo}^{\ell}(z)$, the first order approximation to the eigenvalues $\varepsilon_{n,Jm}$ of Eq. (6.11) are then given by

$$\varepsilon_{n,Jm} = \frac{2M}{\hbar^2} k_z^2 + \frac{\hbar^2}{2I} J_i(J_i + 1) \tag{6.14}$$

$$= \varepsilon_n + \frac{\hbar^2}{2I} J(J + 1) + \sum_{\ell} \langle Jm|P_\ell(\cos\theta)|Jm\rangle\langle n|\tilde{v}_{oo}^{\ell}(z)|n\rangle \tag{6.15a}$$

$$= \varepsilon_{n,Jm}^{(0)} + \varepsilon_{n,Jm}^{(1)} \tag{6.15b}$$

where ε_n is a bound state eigenvalue of the isotropic component $v_{oo}^{o}(z)$ and

$$\varepsilon_{n,Jm}^{(0)} = \varepsilon_n + \frac{\hbar^2}{2I} J(J + 1) \tag{6.16}$$

$$\varepsilon_{n,Jm}^{(1)} = \sum_{\ell} \langle Jm|P_\ell(\cos\theta)|Jm\rangle\langle n|\tilde{v}_{oo}^{\ell}(z)|n\rangle \tag{6.17}$$

Thus $\varepsilon_{n,Jm}^{(0)}$ are the zeroth order bound vibration-rigid rotor (BVRR) eigenvalues and $\varepsilon_{n,Jm}^{(1)}$ are the first order perturbation corrections to these induced by the anisotropy of $V_{oo}(z, \theta)$.

Pure DSA and mixed DSA-RMSA resonances are obtained from Eq. (6.11) with $\underset{\sim}{G} \neq (00)$. Making the diagonal approximation with respect to J again, we derive the first order approximation to these resonance energies as

$$\varepsilon_{n,\underset{\sim}{G}Jm} = \frac{\hbar^2}{2M} k_i^2 + \frac{\hbar^2}{2I} J_i(J_i + 1) \tag{6.18}$$

$$\Psi(z, \theta, \phi, \underset{\sim}{R}) = \sum_{\underset{\sim}{GJm}} \chi_{\underset{\sim}{GJm}}(z)\, Y_{Jm}(\theta, \phi)\Phi_{\underset{\sim}{G}}(\underset{\sim}{R}) \tag{6.9}$$

the following set of close coupled equations is derived

$$\left[\frac{d^2}{dz^2} + k_i^2 + \frac{M}{I} J_i(J_i + 1) - (\underset{\sim}{K}_i + \underset{\sim}{G})^2 - \frac{M}{I} J(J + 1)\right] \chi_{\underset{\sim}{GJm}}(z)$$
$$= \sum_{\underset{\sim}{G'J'M'}} \frac{2M}{\hbar^2} \langle Jm | V_{\underset{\sim}{G}-\underset{\sim}{G'}}(z, \theta, \phi) | J'm' \rangle \chi_{\underset{\sim}{G'J'm'}}(z) \tag{6.10}$$

with J_i the initial rotational state, and I the moment of inertia of the rigid rotor. For weakly corrugated surfaces we neglect the off diagonal $\underset{\sim}{G}$ coupling, retaining only the rotational coupling:

$$\left[\frac{d^2}{dz^2} + k_i^2 + \frac{M}{I} J_i(J_i + 1) - (\underset{\sim}{K}_i + \underset{\sim}{G})^2 - \frac{M}{I} J(J + 1)\right] \chi_{\underset{\sim}{GJm}}(z)$$
$$= \sum_{J'm'} \frac{2M}{\hbar^2} \langle Jm | V_{oo}(z, \theta) | J'm' \rangle \chi_{\underset{\sim}{GJ'm'}}(z) \tag{6.11}$$

Since the initial state has $\underset{\sim}{G} = (00)$ we may drop the subscript $\underset{\sim}{G}$ and assume $\underset{\sim}{G} = (00)$ in Eq. (6.11). The possibility of pure RMSA thereby arises, i.e. resonances observed at eigenvalues of Eq. (6.11) with $\underset{\sim}{G} = (00)$ cause effective coupling of the incident beam (usually $J_i = 0$) to higher J states, which correspond to closed channels asymptotically at the value of k_z . The strong rotational inelasticity seen for the asymmetric rotor HD makes this an ideal case in which to see pure RMSA [50], and it has been previously shown that for HD on smooth metal surfaces (Pt(111) [27] and Ag(111) [28]) these resonance states are very well approximated by the first order approximation to the eigenvalues of Eq. (6.11) with $\underset{\sim}{G} = (00)$. We shall denote the laterally averaged interaction potential for the heteronuclear species HD by $\tilde{V}_{oo}(z, \theta)$ in order to distinguish it from that for the homonuclear species H_2 and D_2, denoted by $V_{oo}(z, \theta)$. $\tilde{V}_{oo}(z, \theta)$ is expanded as

$$\tilde{V}_{oo}(z, \theta) = v_{oo}^{o}(z) + \sum_{\ell = 0,1,\ldots} \tilde{v}_{oo}^{\ell}(z)\, P_\ell(\cos\theta) \tag{6.12}$$

approximation of free atomic motion parallel to the surface in the resonant state

$$\hbar^2 k_i^2/2M = \hbar^2 (\underset{\sim}{K}_i + \underset{\sim}{G})^2/2M + \varepsilon_n \qquad (6.7)$$

when ε_n is a bound state eigenvalue of the isotropic laterally averaged potential $V_{oo}(z)$. Deviations from this free particle approximation will occur at degeneracies, when there is strong coupling by one of the periodic components $V_{\underset{\sim}{G}}(z)$. It is then necessary to calculate the two dimensional band structure of the adsorbed particle in order to predict the positions of interfering resonances. This has been used to extract information on the magnitude of the periodic potential components $V_{\underset{\sim}{G}}(z)$ [24, 48].

Equations (6.1) and (6.7) have been applied to the scattering of H_2 and D_2 from dielectrics and graphite [49, 18]. Due to the spherical nature of the homonuclear hydrogen isotopes and the low rotational excitation probabilities it is to be expected that condition (6.7), which neglects the molecular degrees of freedom, will also be valid for H_2 and D_2 to a first approximation. In fact the free atom approximation will be even better for scattering from metals than from dielectrics. But in general, the *internal molecular* degrees of freedom will affect the resonance conditions. This will now be illustrated for a rigid rotating diatomic incident on a corrugated surface.

The generalization of Eq. (1.1) to a diatomic molecule-periodic surface system is

$$V(z, \theta, \phi, \underset{\sim}{R}) = \sum_{\underset{\sim}{G}} V_{\underset{\sim}{G}}(z, \theta, \phi)\, e^{i\underset{\sim}{G}\cdot\underset{\sim}{R}} \qquad (6.8)$$

where the coordinate system is the standard laboratory fixed frame, and a rigid rotor has been assumed so that the dependence on r is dropped. For a flat surface the laterally averaged term must be independent of ϕ, i.e. $V_{oo}(z, \theta)$. When the molecular wave function is expanded in a direct product basis of rotational and diffraction states

Born-Oppenheimer formalism proposed by Levi and Suhl for slow collisions with soft crystals [40] and deserves further attention.

VI. Selective Adsorption Kinematics: The Molecular Case

The kinematics of selective adsorption are determined by two conditions: i) conservation of parallel momentum

$$\underset{\sim}{K}_f = \underset{\sim}{K}_i + \underset{\sim}{G} \tag{6.1}$$

and ii) conservation of total energy

$$E_f = E_{int} + \hbar^2 k_i^2/2M \tag{6.2}$$

where $\underset{\sim}{k}_i = (\underset{\sim}{K}, k_z)$ is the incident particle wavevector with components $\underset{\sim}{K} = (k_x, k_y)$ parallel and k_z perpendicular to the surface, respectively, M is the total mass of the incident particle, E_{int} its internal energy, and $\underset{\sim}{G}$ a reciprocal lattice vector of the surface.

For atom-solid scattering, with the interaction potential expanded as the Fourier sum, Eq. (1.1), the resonance energies are determined by eigenvalues of the close coupled equations:

$$\left[\frac{d^2}{dz^2} + k_i^2 - (\underset{\sim}{K}_i + \underset{\sim}{G})^2\right] \chi_{\underset{\sim}{G}}(z) = \sum_{\underset{\sim}{G}'} U_{\underset{\sim}{G}-\underset{\sim}{G}'}(z)\, \chi_{\underset{\sim}{G}'}(z) \tag{6.3}$$

where

$$U_{\underset{\sim}{G}}(z) = \frac{2M}{\hbar^2} V_{\underset{\sim}{G}}(z) \tag{6.4}$$

and the atomic wave function has been expanded in a plane wave basis

$$\Psi(r) = \sum_{\underset{\sim}{G}} \chi_{\underset{\sim}{G}}(z) \Phi_{\underset{\sim}{G}}(\underset{\sim}{R}) \tag{6.5}$$

with

$$\Phi_{\underset{\sim}{G}}(\underset{\sim}{R}) = A_s^{-1/2}\, e^{i(\underset{\sim}{K}_i + \underset{\sim}{G})\cdot\underset{\sim}{R}} \tag{6.6}$$

and A_s the area of the surface unit cell. In most cases it is sufficient to retain only the diagonal term on the right hand side of Eq. (6.4), giving the usual

fitted slopes of linear log (I/I_0) vs. T_s plots for a range of $0 \rightarrow 1$ and $0 \rightarrow 2$ rotationally inelastic peaks measured at values of E_z not equal to RMSA resonances. These data now do give a consistent value of well depth D and Debye temperature θ_D, also listed in Table 3. However, the well depth of 31.9 meV is considerably smaller than the value of 45 meV extracted from the homonuclear isotopes. In Figure 9 we show the theoretical Debye-Waller correction factors I/I_0 for each rotationally inelastic transition as a function of E_z, the incident energy normal to the surface, calculated assuming a well depth of a) 45.2 meV and b) 31.9 meV. Superimposed on these lines are the experimentally measured Debye-Waller correction factors for all transitions $J = 0 \rightarrow J = 0, 1, 2$. We note that the experimental points fall within the envelope of the calculated values for b), but not for a). Thus although the $0 \rightarrow 0$ and $0 \rightarrow 3$ peaks have an irregular behavior with energy E_z, they do always fall within the range allowed by the total rotational inelasticity at any given E_z. The disagreement of the curves with the experimental values in the upper panel of Fig. 9 is strong evidence against a well depth of 45 meV. Nevertheless, the discrepancy between the internally consistent H_2 and D_2 results of D = 45 meV and the HD result of 31 meV leaves open an interesting and important question for Debye-Waller analysis. We also note that a similar type of result was seen for molecular hydrogen scattering from Pt(111) [47], where the H_2 $0 \rightarrow 0$ data gave a well depth of 72 meV while the HD rotationally inelastic data gave a well depth of 55 meV.

Our conclusion is that simple Debye-Waller theory, Eq. (5.1), appears to work well for H_2 and D_2 and also for HD, if proper allowance is made for the rotational inelasticity, but that the results from the homonuclear and heteronuclear isotopes are quite different. The anisotropic component of the laterally averaged molecule-surface potential is apparently playing an important role here, which has yet to be determined. This is suggested by the adiabatic

diffuse background scattering has been subtracted from the specular peak. The plots show very good linearity over a range of temperatures, showing essentially only the expected deviations at high temperatures due to anharmonic contributions to lattice vibrations (low incident angle plots) and at low temperatures the deviations characteristic of zero point vibrational energy and contamination effects [42] (high incident angle plots). Extrapolation of the linear segments to 0 K gives close to unit reflectivities (83% for H_2, 88% for D_2, 94% for He) indicating a high degree of surface perfection. Figure 6 presents the slopes for each of the least squares fitted lines of Figure 5, plotted as a function of E_z of the incident beam. Equation (5.2) is then used to obtain an estimate of the well depth, D, and surface Debye temperature θ_D. Calculated mean square displacements $\langle u_z^2 \rangle$ at 273 K are also listed. These values are reported in Table 3 where it is apparent that the homonuclear isotopes H_2 and D_2 give a consistent result of D = 45 meV, but slightly different surface Debye temperatures. The latter are greater than or equal to the bulk value, contrary to expectations based on the relative amplitudes of surface and bulk atom motions.

Figure 7 shows the temperature dependence of some of the HD rotationally elastic and rotationally inelastic specular (all $\underset{\sim}{G}$ = (00)) peaks after subtraction of the diffuse background. Efforts were made to use Eq. (5.3) to extract D and θ_D from the temperature dependence of the 0 → 0 peak in the angular and energy ranges where all rotationally inelastic channels are closed (E_i < 11 meV). No consistent results could be obtained, either coincident with, or between RMSA resonances. This is not surprising since the resonances in this region are very strong and closely spaced in energy. Equation (5.3) is only applicable in the region between resonances, which is ill-defined for the 0 → 0 scattering (Fig. 7). When rotationally inelastic channels are open the 0 → 0 peak intensities are much smaller, and are subject to large experimental uncertainties, as are the 0 → 3 intensities. Figure 8 then shows the least squares

where θ_f and θ_i are related for diffractive scattering by

$$E_i\cos^2\theta_f = E_i - \hbar^2(\underset{\sim}{K}_i + \underset{\sim}{G})^2/2M_g \qquad (5.4)$$

and by

$$E_i\cos^2\theta_f = E_i\cos^2\theta_i + \hbar^2[J_i(J_i + 1) - J_f(J_f + 1)]/2I_g \qquad (5.5)$$

for rotationally inelastic scattering. M_g and I_g are the mass and moment of inertia of the gas particle, M_s the crystal atom mass, D the well depth and θ_D the surface Debye temperature. The temperature dependence of Eq. (5.2) is often used to extract an estimate of the well depth, D. Criticisms of this form include the ambiguity in the definition of $\Delta\underset{\sim}{k}$, i.e. whether this should be measured at the potential minimum or in the repulsive region [39], and the assumption that the incoming particle collides with only one surface atom, [41, 44] which is certainly not the case for large species such as Ne and H_2 [41, 45]. The question of the validity of Eq. (5.1) itself for atomic scattering was investigated by Levi and Suhl [40], who showed that for fast collisions the equation does hold under either completely coherent or completely incoherent lattice motion and the assumption of pairwise interactions. Thus Debye-Waller theory is applicable to both neutrons and electrons by virtue of the short collision times involved. However, for the majority of atomic and molecular scattering, the collision time is of the same order as the characteristic vibration time of the crystal. According to the criterion of Levi and Suhl [40], the scattering of H_2 from Ag(111) is actually a borderline case.

With the above caveat concerning the Debye-Waller factor in mind, but lacking a more suitable alternative, we have analyzed the temperature dependence of the specular rotationally elastic scattering of H_2, D_2 and rotationally inelastic scattering of HD from Ag(111) with the simplest model, Eqs. (5.2-5.3). Figure 5 shows the linear dependence of the logarithms of the specular reflectivities versus surface temperature at various incident angles for H_2, D_2, and He. The

used in X-ray scattering [37], and more recently in neutron scattering and in LEED [38]

$$\begin{aligned} I/I_o &= \exp(-\langle(\underset{\sim}{u}\cdot\Delta\underset{\sim}{k})^2\rangle \\ &\approx \exp(-\langle u_z^2\rangle\Delta\underset{\sim}{k}^2) \end{aligned} \tag{5.1}$$

Here I is the experimentally measured intensity at a fixed surface temperature T_s, I_o the hypothetical intensity for a stationary lattice at 0 k, $\Delta\underset{\sim}{k} = \underset{\sim}{k}_f - \underset{\sim}{k}_i$ the wavevector change of the atom upon collision with the surface and $\langle\underset{\sim}{u}^2\rangle$ the mean square displacement of a surface atom at T_s. There has been much controversy over the applicability of such a Debye-Waller factor to atomic and molecular scattering from surfaces [39-45]. The simplest approach is to evaluate $\Delta\underset{\sim}{k}$ at the potential minimum, thereby including the effect of a thermally averaged attractive well (Beeby correction [46]) and to evaluate $\langle\underset{\sim}{u}^2\rangle$ assuming i) collision with a single surface atom ii) $\langle\underset{\sim}{u}^2\rangle$ is dominated by its normal component iii) harmonic lattice motion and iv) a Debye model for the solid so that $\langle u_z^2\rangle = 3\hbar^2 T_s/M_s k_B \theta_D^2$. The resulting expression for specular scattering is

$$I/I_o = \exp[-24\, M_g(E_i\cos^2\theta_i + D)\, T_s/M_s k_B \theta_D^2] \tag{5.2}$$

and for diffractive or rotationally inelastic scattering

$$I/I_o = \exp\left[-\frac{6\, M_g T_s}{M_s k_B \theta_D}\,(E_i\cos^2\theta_i + D)\left(1 + \sqrt{\frac{E_i\cos^2\theta_f + D}{E_i\cos^2\theta_i + D}}\right)^2\right] \tag{5.3}$$

were ca. 8% for He and 5% for H_2 using 300 K nozzle expansions. They correspond to Debye-Waller corrected reflectivities (i.e. extrapolated to T_s = 0 K) of greater than 80%.

The azimuthal orientation of the crystal was calibrated by optimizing hydrogen diffraction along the <11$\bar{2}$> and <10$\bar{1}$> symmetry directions. Azimuthal settings falling between these two angles (0^o and 30^o) were set using a pointer and scale attached directly to the crystal mount. This pointer could be set to better than 0.2^o by using a remote telescope to read the angle scale. Polar detector and crystal angles were set to better than 0.05^o.

In each experimental session, beam characterizing time-of-flight measurements were taken before and after any beam scattering measurements. Three different beam energies were used for each isotope, shown in Table 2. p-hydrogen and o-deuterium were only available for the beams of lowest energies (nozzle size 12μ). Two types of scattering data were collected: 1) angular distributions obtained by scanning the detector at 0.2^o increments for fixed incident angle and 2) peak intensity scans obtained by measuring the maximum intensity of a given diffraction peak after incrementing the incident angle by ca. 0.2^o. In practice, DSA data was collected by alternately moving the crystal polar angle by ca. 0.2^o, and then scanning the detector through the specular peak with the computer recording in real time the peak intensity and corresponding incident and scattering angles with respect to the surface normal. The peak heights determined in this manner include contributions from both coherently scattered particles and the diffuse inelastic background.

V. Debye-Waller Analysis

Inelastic attenuation of elastic atom-surface scattering intensities by thermal vibrations and zero point motion of the surface is usually analyzed by rescaling with a Debye-Waller attenuation factor analogous to that originally

o-D_2 to that of n-D_2. Note also the disappearance of the J = 1 → 3 peak for D_2 after conversion. Thus the successful generation of a pure J = 0 beam is confirmed. The generation of beams richer in ground rotational state molecules can also be directly demonstrated by detecting a small increase in beam translational energy after conversion due to the extra rotational energy relaxing to the translational degree of freedom, as shown for hydrogen in Figure 4.

IV. Experimental Procedure

The single crystal surface Ag(111) was spark-cut from a 99.999% Ag boule and initially polished at the Cornell Materials Preparation Laboratory. It was subsequently repolished in our laboratory with very fine cerium oxide powder, and electro-chemically etched with a saturated chromic acid-10% HCl solution [36] to remove the damaged topmost layers which result from mechanical polishing. The oxide layer formed from this chemical treatment was removed with a 10% HNO_3 solution. The orientation of the crystal was checked by Laue X-ray back-reflection, and was found to be within 0.5^o of the (111) plane. The underside of the crystal disc was spotwelded to two 1mm thick Pt wires, which were attached to the manipulator through two tungsten rods. A Chromel-Alumel thermocouple was also spotwelded to the back of the crystal. The crystal was resistively heated or conductively cooled through the Pt support wires. Temperature regulation was achieved with a home built circuit which controls the current source.

After the initial bake-out, the crystal was subjected to several cycles of Ar^+ sputtering (2 uA at 500 V for 10 min.) until no appreciable contamination could be detected with a single-pass cylindrical mirror analyzer Auger spectrometer. The crystal was then annealed at 600 K for one hour to remove sputter damage. The success of this annealing procedure was verified by the fairly uniform He and H_2 reflectivities which were measured at several points along the crystal. Typical reflectivities at $\theta_i = 50^o$ with the surface at room temperature

The values of the experimental bound state energies for p-H_2, n-H_2, o-D_2, and n-D_2 are listed in Table 4. The small energy differences, ΔE_n, arising between the n-H_2 (n-D_2) and p-H_2 (o-D_2) results are due to the slight shifts of the $J \neq 0$ $m \neq 0$ resonance energies relative to $|J,m\rangle = |0,0\rangle$. The normal hydrogen (deuterium) results represent a weighted superposition of the $|J,m\rangle = |0,0\rangle$, $|1,0\rangle$, and $|1,\pm1\rangle$ resonances. Although the ΔE_n's are just somewhat larger than the standard deviations, they are not artifacts due to systematic drifts. This was confirmed by taking data for p-H_2 and n-H_2 sequentially, without changing any other experimental conditions. This was accomplished utilizing the bypass value that was intentionally built into the p-H_2 (o-D_2) generator. Note that since n-D_2 contains only 33% $J = 1$ D_2, the level shifts between o-D_2 and n-D_2 are smaller than those between p-H_2 and n-H_2. A more complete discussion of these energy shifts is presented in our paper dealing with the anisotropic component of the laterally averaged hydrogen/Ag(111) potential [13].

VIII. Analysis of Bound State Data From DSA Resonances: p-H_2/o-D_2

A. Assignment of Quantum Numbers

For o-D_2 and p-H_2 the J,m dependent shifts of the bound state levels are equal to zero and the DSA resonance positions provide a direct measurement of the eigenvalues of the isotropic component $v^0_{00}(z)$ of the laterally averaged potential Eqs. (6.16 and 6.18 with $J = J_i = 0$). At the present time there are two ways to generate a one dimensional gas-solid potential $v^0_{00}(z)$ from the spectrum of its eigenvalues $\{\varepsilon_n\}$: either by fitting any one of several model potentials, or by using a modified RKR procedure to generate a set of turning points together with assumption of the asymptotic form $v^0_{00}(z) \sim -C_3/(z-z_0)^3$, Eq. (1.2) [30]. However, in each case it is necessary to first have unambiguous quantum number assignments for the levels $\{\varepsilon_n\}$. This is facilitated by independent knowledge of the

the well depth. When however, as is the case here, it is not clear that standard Debye-Waller analysis is valid and isotopic Debye-Waller studies give inconsistent results for the well depth (Section V), quantum assignments and a crude estimate of the well depth may usually be obtained by simultaneous fitting of different isotopic data for the higher vibrational levels to the asymptotic expression of Le Roy [30]

$$|\varepsilon_n|^{1/6} = 2.02176\ C_3^{-1/3}\ (\eta_d - \eta) \qquad (8.1)$$

where the mass reduced vibrational quantum number is $\eta = (v + \frac{1}{2})/\sqrt{m}$, and η_d is the value of η at the dissociation limit.

Figure 17 shows the Le Roy plot for four different sets of simultaneous assignments for the H_2 and D_2 levels. We note that with the exception of the lowest bound state of hydrogen, the plots are highly linear over the entire range of measured bound states with equal slopes for both species, indicating that Eq. (8.1) is valid over the measured range of energies. The lowest vibrational level for H_2 drops below the limiting slope. In each case best straight lines are fit separately for the two isotopic species to test their closeness. The gradients and intercepts are shown in Table 5. Assignments (a) and (d) are both very close, while (b) and (c) clearly do not give simultaneous fits to Eq. (8.1) for both isotopes, and so can be rejected. Any other possibilities show poorer correlation than these. The assignments (a) and (d) give very different positions for the well depth which is well illustrated by the behavior for the bound state of both isotopes at $\sim$ -10 meV. For (a) this H_2 level has $n = 2$ and D_2 level $n = 3$. This assignment gives a well depth of $\sim$ 32 meV from the model potential fittings shown later. The Y-intercept of the fitted lines in (a) provides an upper bound of $\sim$ 37 meV for the well depth, and implies one unobserved deeper level for D_2 and none for H_2. The slope gives a crude estimate

of C_3, which we obtain as 983 ± 37 meV-Å^3 from (a). For (d) the H_2 level at ∿ -10 meV has n = 4 and the D_2 level n = 6. This implies two unobserved deeper levels for H_2 and four for D_2, and yields a well depth of ∿ 60 meV.

It is clear that this is a rather unusual situation in that the simultaneous isotopic fitting procedure is not on its own sufficient to distinguish between two very different quantum number assignments. This is a consequence of the mass ratios, in particular that $n_1(M_{H_2}^{\frac{1}{2}}) \sim n_2(M_{D_2}^{\frac{1}{2}})$ where n_1 and n_2 are both small integers ($n_1 = 3$, $n_2 = 2$). Fortunately, we can now use the rotationally inelastic transition probabilities for HD to give a crude but independent estimate of the well depth, which is sufficient to distinguish between the values of 30 and 60 meV. Scattering calculations show that the gross features, in particular the energy dependence of the relative rotational transition probabilities, are not very sensitive to the anisotropy of the potential $\tilde{V}_{oo}(z, \theta)$ for HD, but are strongly affected by large variations in the well depth [13, 47]. In the next section we present several model potentials used in the calculations and then compare the results of these quantum scattering calculations using potential parameters obtained by least square fits to assignments (a) and (d), to the experimental rotationally inelastic transition probabilities for HD.

B. The Isotropic Potential $v_{oo}^o(z)$

The following four model potentials were used to fit the bound states ϵ_n of $v_{oo}^o(z)$ for H_2 and D_2:

i) Morse potential

$$v_{oo}^o(z) = D \{\exp[-2\alpha(z-z_e)] - 2\exp[-\alpha(z-z_e)]\} \qquad (8.2)$$

where D is the well depth, α the inverse range parameter and z_e the equilibrium position.

ii) Lennard-Jones 9-3 potential

$$v^o_{oo}(z) = 3^{3/2}\, D/2\, \{\, [\sigma/(z+z_o)]^9 - [\sigma/(z+z_o))]^3 \,\} \tag{8.3}$$

where D is the well depth and λ the range parameter. The potential minimum is given by $z_e = 3^{1/6}\sigma - z_o$.

iii) Variable exponent potential (VEP) [52]

$$v^o_{oo}(z) = D\, \{\, [1 + \lambda/p(z-z_e)]^{-2p} - 2\, [1 + \lambda/p(z-z_e)]^{-p} \,\} \tag{8.4}$$

where D is the well depth, λ is a inverse range parameter, $-1 \leqslant 1/p \leqslant 1$, and z_e is the equilibrium position.

iv) Exponential-3 potential [53]

$$\begin{aligned} v^o_{oo}(z) &= A\, e^{-bz} - f(z)C/z^3 \\ A &= 3\, De^{bz_e}/(bz_e-3) \\ C &= bz_e^4\, D/(bz_e-3) \\ f(z) &= 1-(2z/a_o(1 + z/a_o) + 1)\, e^{-2z/a_o} \end{aligned} \tag{8.5}$$

where D and z_e are the well depth and equilibrium position when $f(z) = 1$, and b is a range parameter. For $f(z) \neq 1$ these values and eigenvalues of the potential are determined numerically using a Numerov-Cooley integrator. $f(z)$ is a cut-off function for the z^{-3} term designed to go smoothly from $f(z) = 1$ at some large z to $f(z) = 0$ at $z = 0$ [54].

The Morse potential has a simple form and analytical eigenvalues but it decays too fast in the long range attractive region. The 9-3 potential shows the correct z^{-3} dependence in the attractive component but the z^{-9} repulsive term is arbitrary. Analytic eigenvalues have been obtained in the WKB approximation for this [55] (accurate to 1%). Both of these are 2-parameter potentials. The variable exponent potential is a 3-parameter

generalization of the Morse potential [52] which has had considerable success in fitting atom-surface and molecule-surface vibrational spectra. Approximate analytical eigenvalues have also been derived for this potential (also good to 1%) [52]. Finally, the exponential-3 potential is a 3-parameter potential which displays the correct asymptotic form expected from theoretical analysis at both large and small z. This is the most realistic model potential, but has the practical disadvantage that no known analytical expression exists for its eigenvalues, which must be solved for numerically.

The potential parameters are determined by simultaneous fitting of the p-H_2 and o-D_2 bound state energies, which are listed in Table 6. Table 7 displays the experimental and calculated eigenvalues for the four fitted potential forms. The quantity χ^2 is used to compare the quality of the fit:

$$\chi^2 = \sum_{\nu} [(E_\nu - E_\nu^c)/\sigma_\nu]^2 \qquad (8.6)$$

with values of χ^2 calculated separately for each isotope and then added to give an overall value for the simultaneous fit. As expected, the two parameter potentials give poorer fits, with the Morse potential worst of all and 9-3 somewhat better. The variable exponent potential is better than the Morse potential by an order of magnitude, and gives a fit comparable to that of the exponential-3 potential. The four best fit potentials are shown in Figure 18.

C. Rotationally Inelastic Quantum Scattering Calculations for HD: Effect of Well Depth

Quantum scattering calculations were performed for interaction of HD with a flat surface using the laterally averaged interaction potential obtained by transformation of the symmetric rotor-surface potential, Eq. (6.21), to the offset center of mass

$$z = z' - \delta \cos\theta \qquad (8.7)$$

where z', z are equal to the normal distance from the surface to the geometric center and center of mass of HD, respectively, and δ is the offset of the center of mass from the geometric center. This results in

$$\tilde{V}_{oo}(z, \theta) = v^0_{oo}(z + \delta\cos\theta) + v^2_{oo}(z + \delta\cos\theta)\, P_2(\cos\theta) \qquad (8.8)$$

$$= v^0_{oo}(z) + \sum_{\ell = 0,1,\ldots} \tilde{v}^{\ell}_{oo}\, P_{\ell}(\cos\theta) \qquad (8.9)$$

In our previous calculations for HD [27, 28] the simplest possible form of the homonuclear anisotropic term $v^2_{oo}(z)$ was used, i.e. $v^2_{oo}(z) = \beta\, v^0_{oo}(z)$. Although this is insufficient for a complete and consistent description of the rotational cross sections for all these isotopes, H_2, D_2, and HD, this crude form is adequate to investigate the difference between a well depth of 30 meV and one of 60 meV since the anisotropy is small.

The scattering calculations were carried out using the Wigner R-matrix, with an L^2 basis of 6 rotational x 60 translational functions [56].

Figure 19 shows the rotational transition probabilities for assignments (a) (well depth = 31.535 meV) and (d) (well depth = 59.941 meV) calculated using the VEP potential. Also included are the deconvoluted pointwise experimental transition probabilities, including subtraction of the diffuse background, instrumental and energy deconvolution, and Debye-Waller corrections [13]. Since the latter was performed at incident angles incremented by 5^o, resonance structures were not resolved. Experimental values have been scaled to give a total cross section of unity. Gross features of the calculated rotational transition probabilities are similar for all four model potentials with a given well depth. Figure 19 and calculations performed at intermediate well depths (e.g. D = 43 meV [28]) show that two features sensitive to the well depth are i) the energy of cross-over for the $J_i = 0 \rightarrow J = 1$ and $J_i = 0 \rightarrow J = 2$ transition probabilities and ii) the magnitude of the $J_i = 0 \rightarrow J = 3$ transition probability. It is clear that there is significantly better

agreement with the experimental results when D = 31.535 meV (Fig. 22b) than when D = 59.941 meV (Fig. 22a). Thus we conclude that the well depth is ∿30 meV and that assignment (a) is the correct assignment for the bound levels of the homonuclear isotopes. These conclusions are fully consistent with the level assignments and isotropic (VEP) potential that have recently been determined for H_2/Ag(110) [57].

IX. Corresponding States Analysis for Physical Adsorption

Vidali, Cole and Klein [31] have recently proposed a principle of corresponding states for the laterally averaged physisorption potential which, when taken with the known asymptotic form Eq. (1.2) gives a reduced Bohr-Sommerfeld quantization relation

$$J(\varepsilon_n^r) = (n + 1/2)b \tag{9.1}$$

$$= \int [\varepsilon_n^r - g(x)]^{\frac{1}{2}}\, dx \tag{9.2}$$

$$b = \hbar\pi/[C_3^{1/3}\, D^{1/6}(2M)^{\frac{1}{2}}] \tag{9.3}$$

where $\varepsilon_n^r = \varepsilon_n/D$ is a reduced energy and g(z) is a reduced potential

$$v_{oo}^o(z) = Dg(z^*) \tag{9.4}$$

$$z^* = (z-z_e)\,(D/C_3)^{1/3} \tag{9.5}$$

This has been used by Vidali et al. with a reduced exponential-3 potential

$$g(z^*) = (3/(u-3))\exp(-z^*u/x_m) - 1/(z^* + x_m)^3 \tag{9.6}$$

where $x_m = (1-3/u)^{1/3}$ to fit all known bound state resonance data for hydrogen and noble gas scattering from surfaces to plots of $J(\varepsilon_n)$ vs. ε_n. It is found that all alkali halide data are characterized by a parameter u = 5.25 while the H_2/noble metals and noble gases/graphite systems are characterized by a value of u = 6.5.

The success of this principle of corresponding states reflects the dominance of the attractive component of $v_{oo}^o(z)$ in determining bound state energies. Since from the high linearity of the LeRoy plot, Fig. 17, this is

also true for the isotropic component $v_{00}^{o}(z)$ of the laterally averaged potential for molecular hydrogen on Ag(111), the bound states of $v_{00}^{o}(z)$ are expected to comply with the reduced quantization plots obtained by Vidali et al. [31] from atomic scattering data. Fig. 20 shows the reduced quantities $J(\varepsilon_n)$ (Eq. 9.1) plotted against ε_n for each of the quantum number assignments (a) and (d). The value of C_3 used was determined from the slope of the Le Roy plots, Eq. (8.1). The solid and dashed lines represent the reduced plots of Vidali et al. obtained using Eqs. (9.2) and (9.6) with $u = 6.5$ and 5.25, respectively. Assignment (a) is in good agreement with the $u = 6.5$ curve appropriate to noble metals, while points from assignment (d) lie somewhat higher than the $u = 5.25$ curve appropriate to alkali halides, which renders this assignment less plausible. The point of this comparison is not to derive a value of u, which is specific to the parametric form, Eq. (9.6), but to match the bound state behavior of the $H_2(D_2)$/Ag(111) system against that of other species physisorbed on similar surfaces but with different well depths. Thus it is of special interest and value to this study because of the particular combination of isotopic masses, which rendered the results of an isotopic study based on the Le Roy analysis inconclusive.

Figure 21 shows the reduced exponential-3 potential, Eq. (9.6), for $u = 6.5$ plotted together with the reduced variable exponent potential, Eq. (8.4), derived from assignments (a) and (d) (see Table 6). The attractive portion of the VEP potential with well depth $D = 31.535$ meV is nearly coincident with that of the reduced exponential-3 potential, as expected from the degree of agreement shown in Fig. 20.

X. Thermal Desorption Experiments

Efforts were also made to obtain an independent estimate of the hydrogen/Ag(111) well depth from thermal desorption and modulated beam measurements.

The experimental observation was that no substantial adsorption or desorption of H_2 (or D_2) was detected at temperatures $\gtrsim$ 19 K, the lowest surface temperature that could be reached with our crystal mount. Attempts were also made to examine reflected molecule waveforms from a 19 K surface; no noticeable demodulation was observed. These facts are only consistent with the well depth assignment being D = 32 meV, as the alternate D $\simeq$ 60 meV well depth would lead to appreciable hydrogen adsorption. This can be demonstrated using the first order rate equation which, for a constant temperature ramping rate β, relates this activation energy for desorption to the peak desorption temperature [58]:

$$E_a/RT_p^2 = (\nu_1/\beta)\ \exp(-E_a/RT_p) \qquad (10.1)$$

where E_a is the activation energy, T_p the peak desorption temperature, and ν_1 the pre-exponential factor for first order desorption. This equation was solved numerically using the experimental temperature ramping rate of $\sim$ 1.3 K/sec and an assumed (typical) frequency factor, $\nu_1 = 10^{13}\ sec^{-1}$. The calculated peak desorption temperatures which result from this exercise are ca. 13 K for a well depth of 32 meV and 24 K for D = 60 meV-- consistent with our earlier conclusion from the Le Roy analysis and rotationally inelastic HD scattering that the lower value of the well depth is the correct assignment.

XI. Summary and Conclusion

In this paper we have presented a comprehensive study of the spatially isotropic component of the laterally averaged molecular hydrogen/Ag(111) physisorption potential. Our analysis began by mapping out the diffractive and rotationally mediated selective adsorption scattering resonances for n-H_2, p-H_2, n-D_2, and o-D_2 in the K_x-K_y reciprocal lattice plane. This was carried out as a function of incident polar angle for several crystal azimuths and beam energies. The resonances show small energy shifts and linewidth changes between p-H_2 and n-H_2, and between o-D_2 and n-D_2, respectively, which

are a direct consequence of the anisotropic component of the laterally averaged molecule-surface potential. The detected differences represent an average over the $|J,m\rangle$ state distributions present in the incident n-H_2 and n-D_2 beams. The ability to resolve DSA dips on Ag(111), a surface of extremely low corrugation, is important in that it suggests that future bound state studies should be feasible on a much wider selection of crystalline surfaces than previously thought possible. Measurements on Pt(111) also support this contention [14].

The experimentally determined bound state energies for o-D_2 and p-H_2, i.e. $|J,m\rangle = |0,0\rangle$, have been used to obtain the unperturbed bound eigenvalues of the potential well. Best fit Lennard-Jones, Morse, variable exponent, and exponential-3 potentials having well depths of $\sim$32 meV are derived from the data. Unfortunately, this well depth assignment could not be made exclusively on the basis of a Le Roy type analysis [30], as two possible quantum number assignments, corresponding to well depths of ca. 32 and 60 meV, were indicated. Comparison of experimental HD rotationally inelastic transition probabilities with results from theoretical scattering calculations for each well depth indicates that the true well depth is $\sim$32 meV. This conclusion is further supported by thermal desorption measurements, and is consistent with a reduced ("universal") potential which has been formulated for closed-shell/noble metal physisorption systems [31]. The derived isotropic potential is also in excellent agreement with recent ab initio predictions for H_2/Ag(111) [59].

Standard Debye-Waller analysis fails to give a consistent well depth for all three isotopes H_2, D_2 and HD. Since this system involves a borderline fast/slow collision with a soft lattice, according to the criteria proposed by Levi and Suhl [40], it is not clear that the standard Debye-Waller analysis should be valid. The significant difference between the heteronuclear result and that for the homonuclear isotopes indicates that the anisotropic component of the potential may be of importance to thermal attenuation in a manner which

is not well understood at the present time.

We close by noting that the isotropic potential determined in this paper plays an essential role in subsequent studies dealing with the spatially anisotropic [13] and periodic [60] component of the hydrogen/Ag(111) potential.

Acknowledgments

The authors wish to thank K. D. Gibson and Y. W. Yang for their assistance throughout these experiments, and J. C. Light for valuable discussions. This work was supported, in part, by the Office of Naval Research (ONR-N00014-77-C-0240), by the Materials Research Laboratory Program at the University of Chicago (NSF-DMR-7924007), and by a Camille and Henry Dreyfus Young Faculty Grant to S. J. Sibener.

References

[1] H. Hoinkes, Rev. Mod. Phys. 52, 933 (1980).

[2] M. J. Cardillo, Ann. Rev. Phys. Chem. 32, 331 (1981).

[3] I. Estermann and O. Stern, Z. Phys. 61, 95 (1930).

[4] J. E. Lennard-Jones and A. F. Devonshire, Nature (London) 137, 1069 (1936); Proc. Roy. Soc. London A, 158, 253 (1937).

[5] E. M. Lifshitz, Sov. Phys.--JETP 2, 73 (1956).

[6] E. Zaremba and W. Kohn, Phys. Rev. B13, 2270 (1976); J. Harris and P. J. Feibelmann, Surf. Sci. 115, L133 (1982); G. Vidali and M. W. Cole, Surf. Sci. 110, 10 (1981); B.N.J. Persson and E. Zaremba, Phys. Rev. B30, 5669 (1984).

[7] G. G. Kleinman and U. Landman, Phys. Rev. B8, 5484 (1973); E. Zaremba and W. Kohn, Phys. Rev. B15, 1769 (1977).

[8] J. Harris and A. Liebsch, J. Phys. C15, 2275 (1982); J. Harris and A. Liebsch, Phys. Rev. Lett. 49, 341 (1982); A. Liebsch, J. Harris, B. Salanon and J. Lapujoulade, Surf. Sci. 123, 338 (1982).

[9] J. Perreau and J. Lapujoulade, Surf. Sci. 119, L292 (1982); J. Perreau and J. Lapujoulade, Surf. Sci. 122, 341 (1982).

[10] J. Harris and A. Liebsch, Physica Scripta T4, 14 (1983).

[11] N. Esbjerg and J. K. Nørskov, Phys. Rev. Lett. 45, 807 (1980); R. B. Laughlin, Phys. Rev. B25, 2222 (1982).

[12] D. R. Hamaan, Phys. Rev. Lett. 46, 1227 (1981).

[13] K. B. Whaley, C. F. Yu, C. S. Hogg, J. C. Light, and S. J. Sibener, submitted to J. Chem. Phys.

[14] J. P. Cowin, Ph.D. Thesis, University of Chicago, 1981.

[15] H. Hoinkes, H. Nahr and H. Wilsch, Surf. Sci. 30, 363 (1972).

[16] G. Derry, D. Wesner, W. Carlos and D. R. Frankl, Surf. Sci. 87, 629 (1979).

[17] E. Ghio, L. Mattera, C. Salvo, F. Tommasini and U. Valbusa, J. Chem. Phys. 73, 556 (1980).

[18] L. Mattera, F. Rosatelli, C. Salvo, F. Tommasini, U. Valbusa, and G. Vidali, Surf. Sci. 93, 515 (1980).

[19] G. Boato, P. Cantini, C. Guidi, R. Tatarek and G. P. Felcher, Phys. Rev. B20, 3957 (1979).

[20] R. Smoluchowski, Phys. Rev. 60, 661 (1941).

[21] G. Boato, P. Cantini and R. Tatarek, J. Phys. F6, L237 (1976); J. M. Horne and D. R. Miller, Surf. Sci. 66, 365 (1977); J. M. Horne, S. C. Yerkes and D. R. Miller, Surf. Sci. 93, 47 (1980).

[22] N. R. Hill, M. Haller and V. Celli, Chem. Phys. 73, 363 (1982).

[23] A. Liebsch and J. Harris, Surf. Sci. 130, L349 (1983).

[24] H. Chow and E. D. Thompson, Surf. Sci. 59, 225 (1976).

[25] Ph. Avouris, D. Schmeisser and J. E. Demuth, Phys. Rev. Lett. 48, 199 (1982).

[26] S. Andersson and J. Harris, Phys. Rev. Lett. 48, 545 (1982).

[27] K. B. Whaley, J. C. Light, J. P. Cowin and S. J. Sibener, Chem. Phys. Lett. 89, 89 (1982).

[28] C. F. Yu, C. S. Hogg, J. P. Cowin, K. B. Whaley, J. C. Light and S. J. Sibener, Isr. J. Chem. 22, 305 (1982);

[29] R. Schinke, Chem. Phys. Lett. 87, 438 (1982); R. Schinke, Surf. Sci. 127, 283 (1983).

[30] R. J. Le Roy, Surf. Sci. 59, 541 (1976).

[31] G. Vidali, M. W. Cole and J. R. Klein, Phys. Rev. B28, 3064 (1983).

[32] C. A. Becker, Ph.D. Thesis, University of Chicago, 1980.

[33] G. E. Schmauch, A. H. Singleton, Ind. Eng. Chem. 56, 20 (1964).

[34] I. F. Silver, Rev. Mod. Phys. 52, 393 (1980).

[35] J. Andres, U. Buck, F. Huisken, J. Schleusener and F. Torello, J. Chem. Phys. 73, 5620 (1980).

[36] E. R. Jones, J. T. McKinney and M. B. Webb, Phys. Rev. 151, 476 (1966).

[37] R. N. James, The Optical Principles of the Diffraction of X-rays (Bell, London 1967).

[38] R. J. Glauber, Phys. Rev. 98, 1692 (1955); J. B. Pendry, Low Energy Electron Diffraction (Academic Press, London 1974).

[39] F. O. Goodman, Surf. Sci. 65, 37 (1977).

[40] A. C. Levi and H. Suhl, Surf. Sci. 88, 221 (1979).

[41] G. Armand, J. Lapujoulade and Y. Lejay, Surf. Sci. 63, 143 (1977).

[42] J. Lapujoulade, Y. Lejay and G. Armand, Surf. Sci. 95, 107 (1980).

[43] L. Greiner, H. Hoinkes, H. Kaarmann, H. Wilsch and N. Garcia, Surf. Sci. 94, L195 (1980).

[44] H. Hoinkes, H. Nahr and H. Wilsch, Surf. Sci. 33, 516 (1972).

[45] J. Lapujoulade, J. Perreau and A. Kara, Surf. Sci. 129, 59 (1983).

[46] J. L. Beeby, J. Phys. C4, L359 (1971).

[47] J. P. Cowin, C. F. Yu, S. J. Sibener and L. Wharton, J. Chem. Phys. 79, 3537 (1983).

[48] H. Hoinkes, L. Greiner, H. Wilsch in Proc. of 7th Int'l Vacuum Congress and 3rd Int'l Conference on Solid Surfaces, Vienna 1977, Ed. by R. Dobrozemsky et al. (Berger, Vienna (1977)).

[49] D. R. O'Keefe, J. N. Smith, Jr., R. L. Palmer and H. Saltsburg, J. Chem. Phys. 52, 4447 (1970).

[50] J. P. Cowin, C. F. Yu, S. J. Sibener and J. E. Hurst, J. Chem. Phys. 75, 1033 (1981).

[51] C. F. Yu, K. B. Whaley, C. S. Hogg and S. J. Sibener, Phys. Rev. Lett. 51, 2210 (1983).

[52] L. Mattera, C. Salvo, S. Terreni and F. Tommasini, Surf. Sci. 97, 158 (1980).

[53] H. Chow, Surf. Sci. 66, 221 (1977).

[54] J. Harris, private communication.

[55] M. W. Cole, T. T. Tsong, Surf. Sci. 69, 325 (1977).

[56] K. B. Whaley and J. C. Light, J. Chem. Phys. 81, 2144 (1984).

[57] M. Chiesa, L. Mattera, R. Musenich, and C. Salvo, to be published.

[58] P. A. Redhead, Vacuum 12, 203 (1962).

[59] P. Norlander and C. Holmberg, to be published.

[60] K. B. Whaley, C. F. Yu, C. S. Hogg. J. C. Light, and S. J. Sibener, to be published.

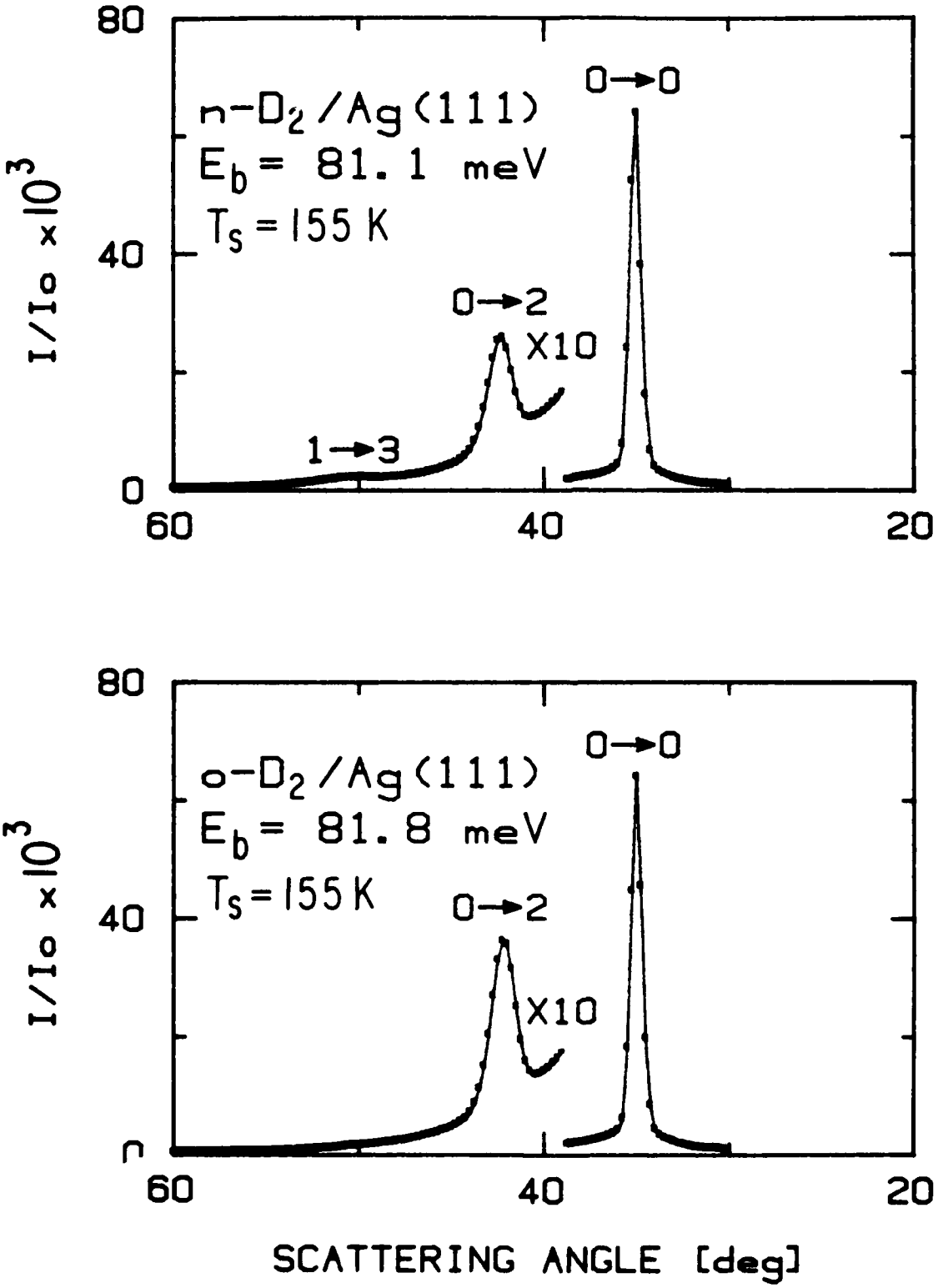
80
40
0
I/Io x10^3
n-D2/Ag(111)
Eb = 81.1 meV
Ts = 155 K
0→0
0→2
X10
1→3
60
40
20
80
40
0
I/Io x10^3
o-D2/Ag(111)
Eb = 81.8 meV
Ts = 155 K
0→0
0→2
X10
60
40
20
SCATTERING ANGLE [deg]

FIGURE 3

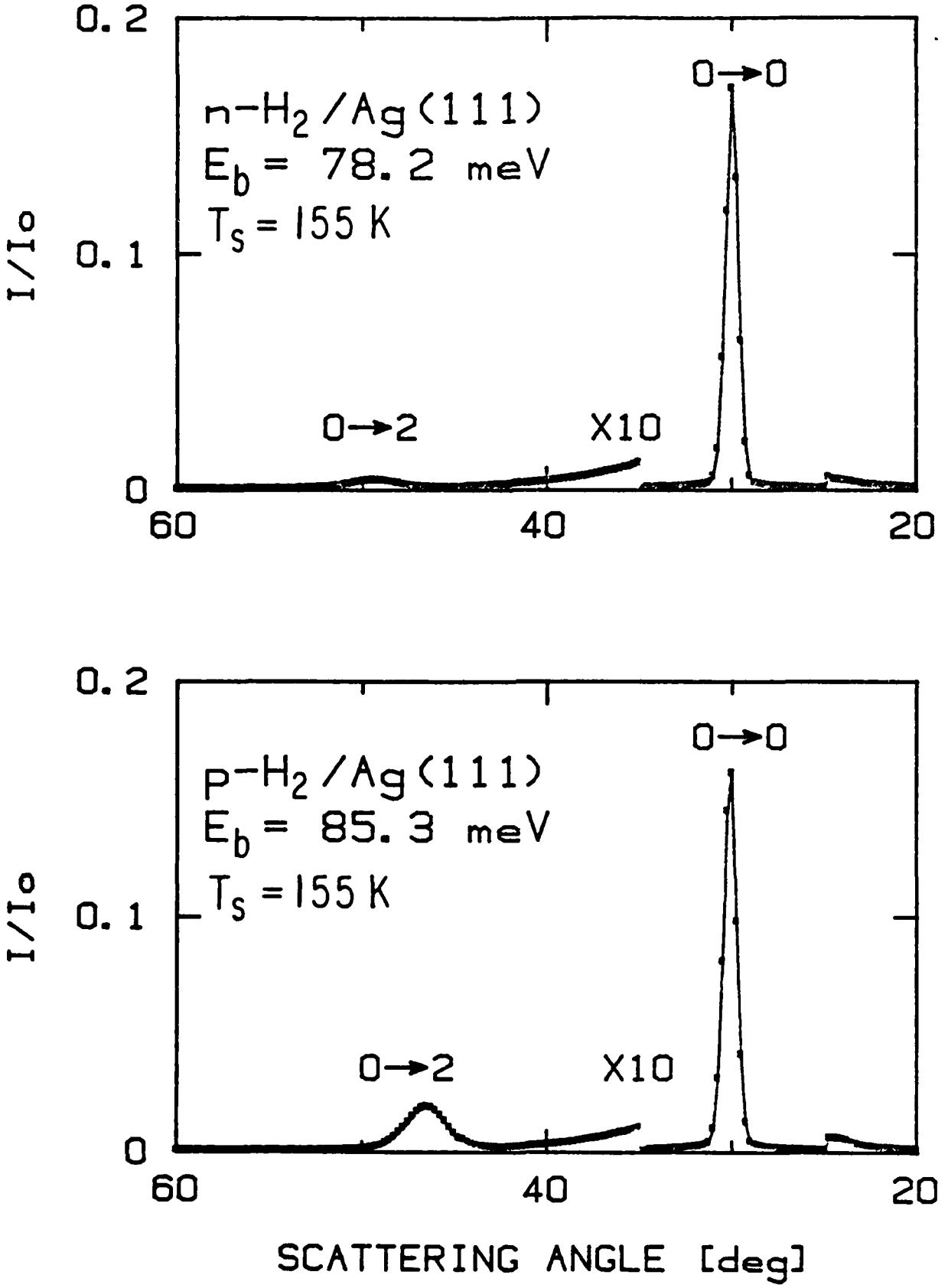
0.2
0.1
0
I/Io
n-H2/Ag(111)
Eb = 78.2 meV
Ts = 155 K
0→0
0→2
X10
60
40
20
0.2
0.1
0
I/Io
p-H2/Ag(111)
Eb = 85.3 meV
Ts = 155 K
0→0
0→2
X10
60
40
20
SCATTERING ANGLE [deg]

FIGURE 2

IN-LINE $p\text{-}H_2/o\text{-}D_2$ CONVERTER

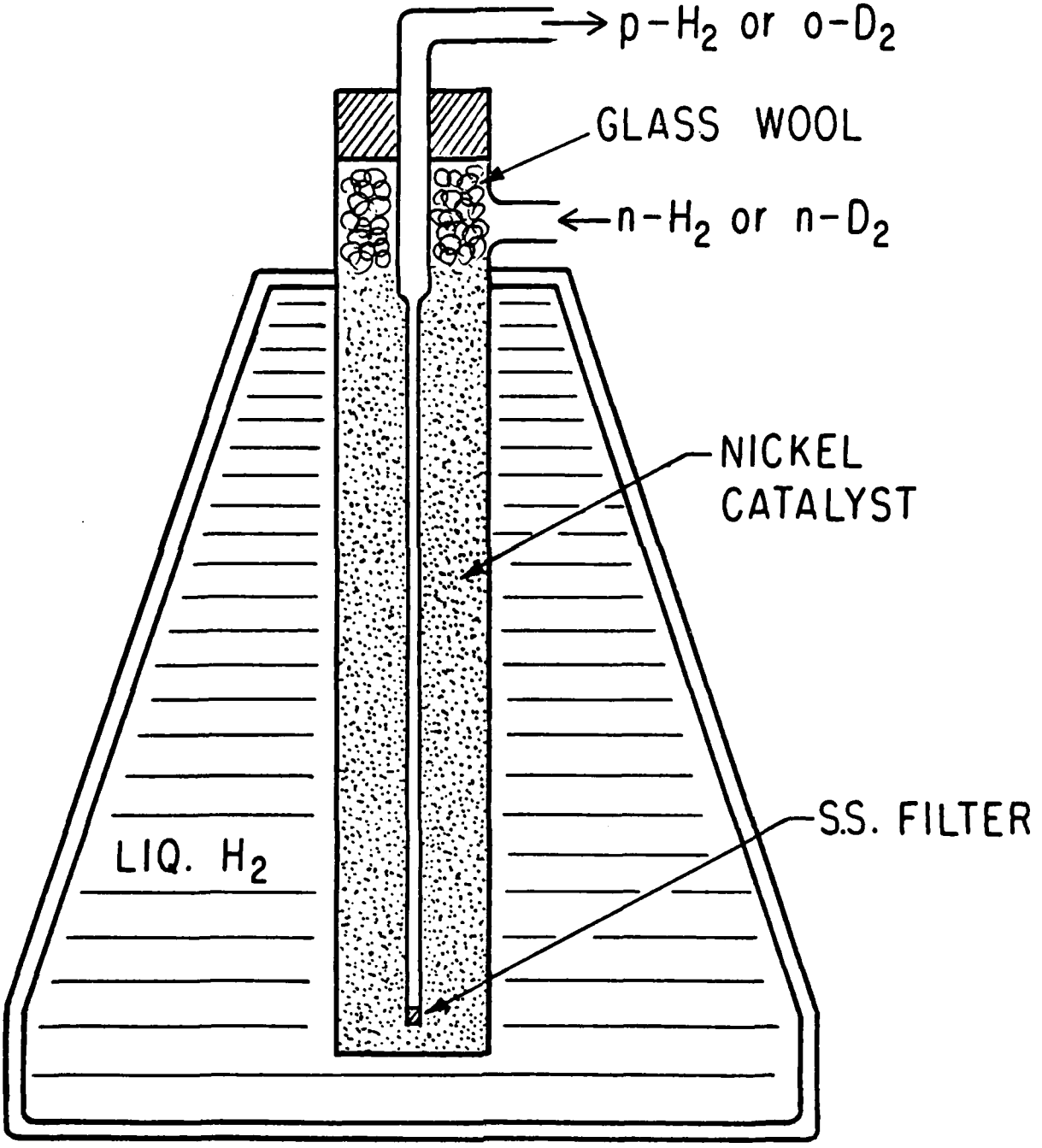

FIGURE 1

Figure 17 Le Roy plots of the p-H_2 (+) and o-D_2 (•) eigenvalues for four different quantum number assignments: a) corresponds to D ∿ 32 meV; b) one extra level for both H_2 and D_2; c) one extra level for H_2 and two extra levels for D_2; d) two extra levels for H_2 and three extra levels for D_2, corresponding to D ∿ 60 meV.

Figure 18 Plots of the four model potentials derived from the experimentally determined p-H_2 and o-D_2 bound state energies on Ag(111).

Figure 19 Comparison of the calculated scattering probabilities for HD/Ag(111) based on D = 59.9 meV (upper) and D = 31.5 meV (middle) with the experimental results derived from angular distributions collected at incident angle increments of 5^o.

Figure 20 $J(\varepsilon)$ defined by Eqs.(9.1-9.3) versus reduced bound state energy for p-H_2 and o-D_2/Ag(111) based on two possible well depths. The D = 31.5 meV values fall on the curve appropriate for closed shell/noble metal adsorption systems.

Figure 21 Comparison of the reduced experimental VEP potentials (based on two possible well depth assignments) with the reduced corresponding states exp-3 potential. The excellent agreement between the D = 31.5 meV VEP potential and the corresponding states potential in the attractive (relevant) region supports the contention that this is the correct well depth for hydrogen/Ag(111).

Figure 10 Specular peak intensity of H_2 scattering from Aq(111) as a function of incident polar angle at two azimuths symmetric about the <11$\bar{2}$> direction. The presence of weak but reproducible dips in these two early (low signal-to-noise) data runs confirmed that diffractive selective adsorption resonances could be observed on Ag(111).

Figure 11 Specular peak intensity of p-H_2 scattering from Ag(111) as a function of incident polar angle for eight successive azimuthal angles.

Figure 12 Selective adsorption loci for p-H_2 plotted in the surface reciprocal-lattice plane. Arc labels denote bound levels (meV) and coupling G vectors. Points represent dips from the resonance spectra. The dashed arc denotes the energy limit for the p-H_2 beam.

Figure 13 Specular peak intensity of o-D_2 scattering from Ag(111) as a function of incident polar angle for seven successive azimuthal angles.

Figure 14 Selective adsorption loci for o-D_2 plotted in the surface reciprocal-lattice plane. Arc labels denote bound levels (meV) and coupling G vectors. Points represent dips from the resonance spectra. The dashed arc denotes the energy limit for the o-D_2 beam.

Figure 15 Specular peak intensity of n-H_2 scattering from Ag(111) as a function of incident polar angle for three beam energies.

Figure 16 Specular peak intensity of n-D_2 scattering from Ag(111) as a function of incident polar angle for three beam energies.

FIGURE CAPTIONS

Figure 1 In-line p-H_2 and o-D_2 converter.

Figure 2 Angular distributions of n-H_2 (upper) and p-H_2 (lower) scattering from Ag(111). The approximate four-fold increase in the $J = 0 \rightarrow 2$ transition probability in the lower panel confirms that the gas has been successfully converted to p-H_2 ($J = 0$ after expansion).

Figure 3 Angular distributions of n-D_2 (upper) and o-D_2 (lower) scattering from Ag(111). The approximate 50% increase in the $J = 0 \rightarrow 2$ transition probability in the lower panel confirms that the gas has been successfully converted to o-D_2 ($J = 0$ after expansion). Also note that the $J = 1 \rightarrow 3$ transition is absent in the lower panel.

Figure 4 Time-of-flight distributions for n-H_2 and p-H_2. The higher terminal velocity of the p-H_2 beam confirms that the p-H_2 converter functions properly.

Figure 5 Debye-Waller plots for H_2, D_2, and He specular scattering from Ag(111).

Figure 6 Linear fits to the slopes of the lines shown in Fig. 5 plotted versus E_z.

Figure 7 Debye-Waller plots for various HD elastic and rotationally inelastic peak intensities versus T_s.

Figure 8 Linear fits to the slopes of the lines shown in Fig. 7 plotted versus E_z.

Figure 9 Theoretical reciprocal Debye-Waller attenuation plots for HD/Ag(111) for two different well depths. Superimposed on the calculated curves are the experimentally determined values. These are designated by numerals which indicate the final rotational quantum state of the scattering transition.

Table 8

Reduced quantities for the "universal physisorption potential".

	(a)			(d)		
	$D = 31.54$ meV $C_3 = 983$ meV-Å^3 $\lambda = 3.148$ Å			$D = 59.94$ meV $C_3 = 829$ meV-Å^3 $\lambda = 2.400$ Å		
	b = .1810			b = .1722		
	n	ε_n	$J(\varepsilon_n)$	n	ε_n	$J(\varepsilon_n)$
	5	.0384	.996	7	.0202	1.292
	4	.0828	.815	6	.0435	1.119
H_2	3	.1737	.634	5	.0913	.947
	2	.3205	.451	4	.1687	.775
	1	.5349	.272	3	.2814	.603
	0	.8161	.091	2	.4294	.431
	b = .1281			b = .1218		
	n	ε_n	$J(\varepsilon_n)$	n	ε_n	$J(\varepsilon_n)$
	7	.0358	.961	10	.0189	1.279
	6	.0758	.833	9	.0399	1.157
	5	.1259	.705	8	.0662	1.035
D_2	4	.2083	.576	7	.1096	.914
	3	.3199	.448	6	.1683	.792
	2	.4588	.320	5	.2414	.670

Table 7

Experimental (E_n) and calculated (ε_n) eigenvalues of the Hydrogen/Ag(111) physisorption potential for four model potentials.

	n	E_n	ε_n: Morse	9-3	VEP	Exp-3
	5	-1.21 ± .06	-.32	-1.46	-.97	-1.09
	4	-2.61 ± .13	-2.11	-2.93	-2.58	-2.58
H_2	3	-5.47 ± .10	-5.48	-5.50	-5.44	-5.37
	2	-10.11 ± .09	-10.42	-9.70	-9.98	-9.93
	1	-16.87 ± .07	-16.94	-16.30	-16.62	-16.63
	0	-25.74 ± .07	-25.03	-26.27	-25.81	-25.67
	χ^2		297	139	31	22
	7	-1.13 ± .05	-.54	-1.68	-1.20	-1.30
	6	-2.39 ± .10	-1.87	-2.75	-2.37	-2.39
	5	-3.97 ± .06	-3.98	-4.33	-4.15	-4.10
D_2	4	-6.57 ± .10	-6.87	-6.62	-6.69	-6.60
	3	-10.09 ± .06	-10.56	-9.83	-10.13	-10.07
	2	-14.47 ± .20	-15.04	-14.24	-14.62	-14.60
	1	----	-20.30	-20.19	-20.33	-20.30
	0	----	-26.36	-28.09	-27.41	-27.20
	χ^2		244	192	14	17
TOTAL χ^2			541	331	45	39

Table 6

Fit parameters for the model potentials. Those listed under (a) with D $\sim$ 32 meV are the correct potentials for Hydrogen/Ag(111).

		D [meV]	s, z_e [Å]	α,λ,β [1/Å]	p
(a)	Morse	29.678		.8717	
	9-3	32.908	2.4651		
	VEP	31.535		1.0646	4.2920
	Exp-3	32.462	1.9883	2.4167	
(d)	Morse	51.628		.8522	
	9-3	73.400	1.9371		
	VEP	59.941		5.0964	1.1124

Table 5

Fitted parameters of the Le Roy plots for four different quantum number assignments. (a)-(d) refer to Figure 19.

	slope $[(meV)^{1/6}(amu)^{1/2}]$	intercept $[(meV)^{1/6}]$			
		(a)	(b)	(c)	(d)
H_2	-2.038	1.823	1.967	1.967	2.111
D_2	-2.049	1.822	1.924	2.026	2.129

Table 4

Experimentally determined bound state energies of p-H_2, n-H_2, o-D_2, and n-D_2 on Ag(111). σ is the standard deviation, m the number of data points and n the assigned quantum number. ΔE_n is the difference between the energies of bound p-H_2 (o-D_2) and (quantum state averaged) n-H_2 (n-D_2).

p-H_2 E_b = 18.57 meV			n-H_2 E_b = 18.09 meV		
n	E_n	σ (m)	E_n	σ (m)	ΔE_n
5	-1.21	.06(11)	-1.12	.05(5)	.09
4	-2.61	.13(22)	-2.52	.07(14)	.09
3	-5.47	.10(45)	-5.35	.09(30)	.12
2	-10.11	.09(42)	-9.91	.09(31)	.20
1	-16.87	.07(28)	-16.55	.11(14)	.32
0	-25.74	.07(2)	-25.53	.21(2)	.21

o-D_2 E_b = 21.68 meV			n-D_2 E_b = 20.71 meV		
n	E_n	σ (m)	E_n	σ (m)	ΔE_n
7	-1.13	.05(11)	-1.17	.12(3)	-.04
6	-2.39	.10(26)	-2.36	.06(6)	.03
5	-3.97	.06(21)	-3.94	.07(9)	.03
4	-6.57	.10(32)	-6.52	.07(10)	.05
3	-10.09	.06(25)	-10.06	.07(7)	.03
2	-14.47	.20(8)	-14.40	.05(4)	.07
2	-15.25*	.04(5)	...	...	...
1	-20.97*	.04(13)	-20.98*	.02(3)	...

*RMSA dips due to J = 0 → 2 transitions

Table 3

Results of Debye-Waller Analysis. D is the derived well depth, θ_D the surface Debye Temperature, and $\langle u_z^2 \rangle$ the mean square displacement at 273 K.

	E_b [meV]	D [meV]	θ_D [K]	$\langle u_z^2 \rangle$ [Å^2]
H_2	77.0	45.0	217	0.0078
D_2	83.5	45.4	238	0.0065
HD	112.8	31.9	228	0.0071
He	65.0	15.0	234	0.0068

Table 2

Beam Parameters. E_b is the incident translational energy, P_n the nozzle stagnation pressure, and D_n the nozzle diameter.

	E_b [meV]	P_n [psig]	D_n [μ]	Δv/v
	77.1	200	20	5.0%
$n\text{-}H_2$	32.3	60	20	5.7%
	18.1	100	12	4.5%
	82.8	280	20	7.0%
$n\text{-}D_2$	36.7	80	20	7.2%
	20.7	90	12	6.6%

Table 1

Calculated incident beam rotational state populations for n-H_2, p-H_2, n-D_2, and o-D_2 and the relative probablities of the J = 0 → 2 scattering transitions. T_r is the rotational temperature of the terminal expansion. W_p and W_s are the scattering probabilities of the J = 0 → 2 and specular peaks, respectively. T_o = 302 K.

	E_b [meV]	T_r [K]	$P_J = 0$	$P_J = 1$	$P_J = 2$	$P_J = 3$	W_p/W_s
n-H_2	78.2	143	21.8	74.5	3.2	0.5	.0059
p-H_2	85.3	139	88.2	0.2	11.6	0.0	.0283
n-D_2	81.1	118	42.5	31.4	24.0	2.0	.0527
o-D_2	81.8	116	63.1	2.1	34.4	0.1	.0837

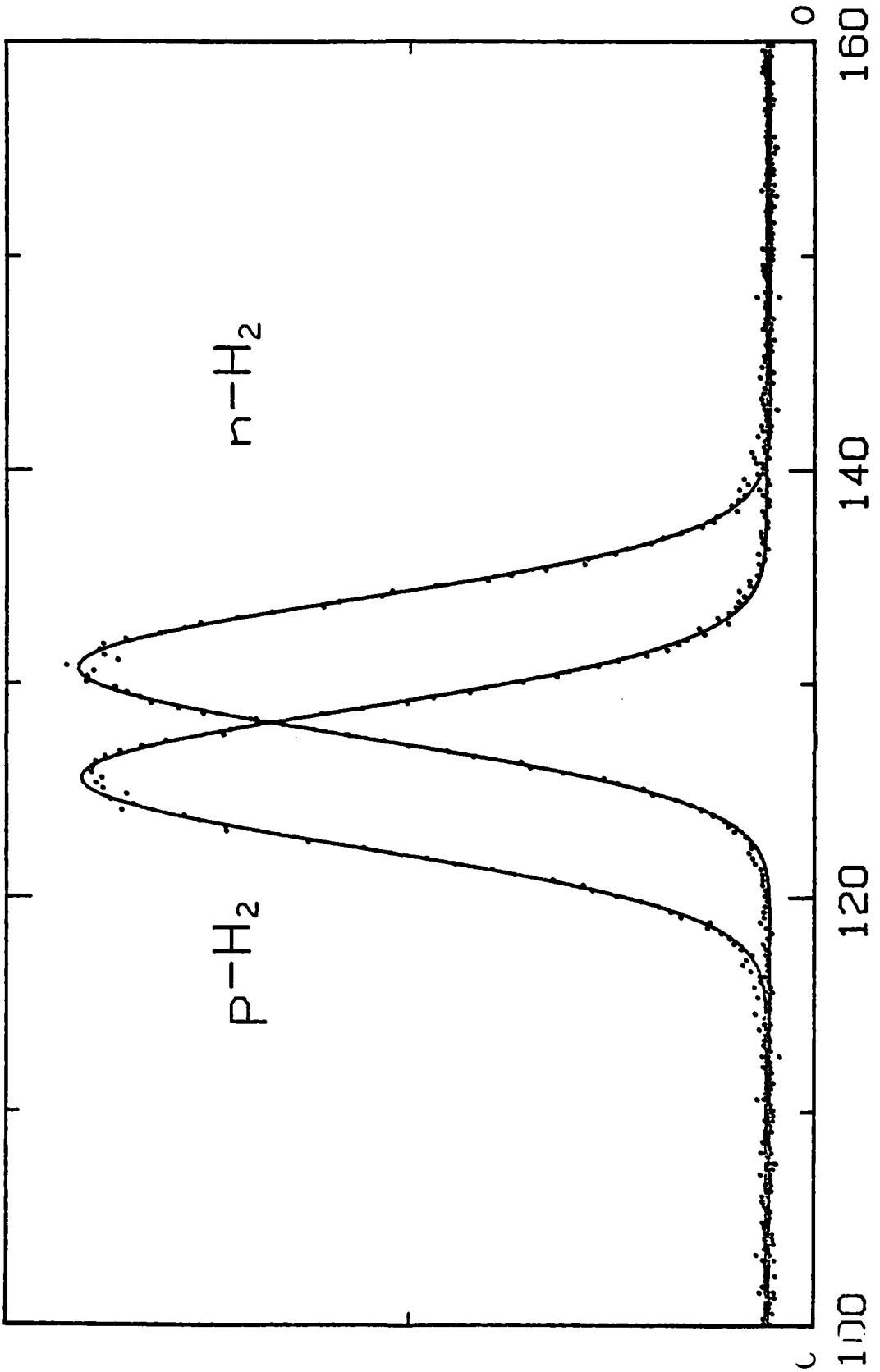

FIGURE 4

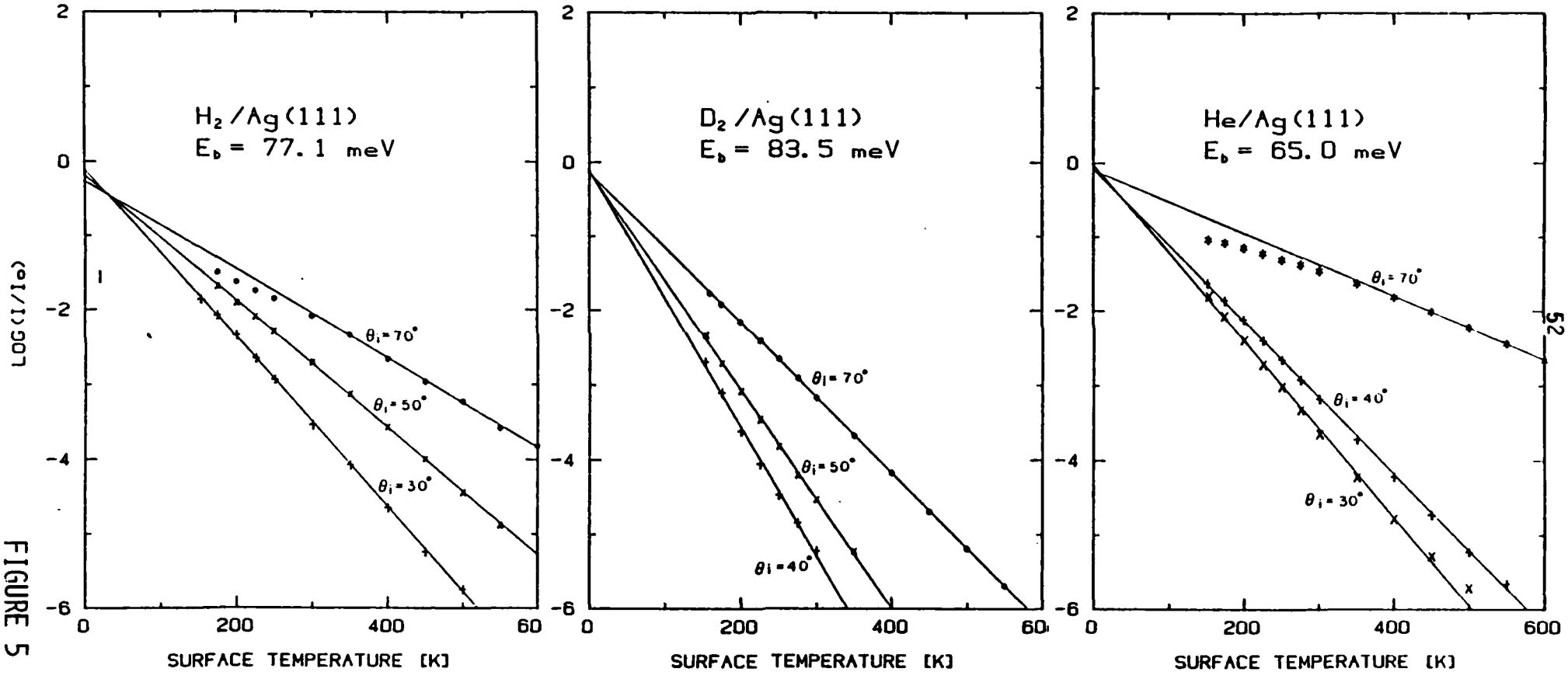
H_2 /Ag(111)
E_b = 77.1 meV
θ_i = 70°
θ_i = 50°
θ_i = 30°
D_2 /Ag(111)
E_b = 83.5 meV
θ_i = 70°
θ_i = 50°
θ_i = 40°
He/Ag(111)
E_b = 65.0 meV
θ_i = 70°
θ_i = 40°
θ_i = 30°
LOG(I/I0)
SURFACE TEMPERATURE [K]
SURFACE TEMPERATURE [K]
SURFACE TEMPERATURE [K]

FIGURE 5

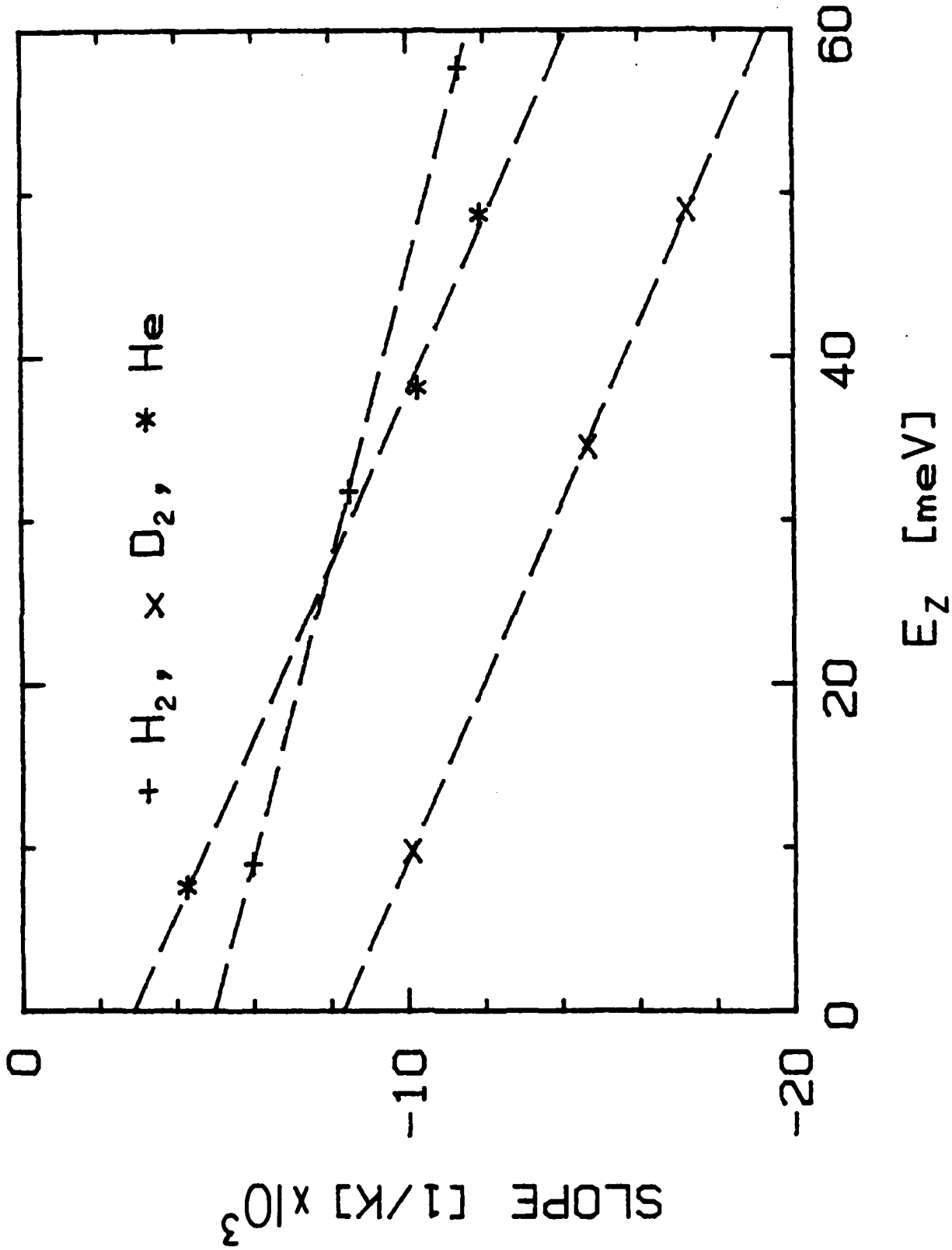

FIGURE 6

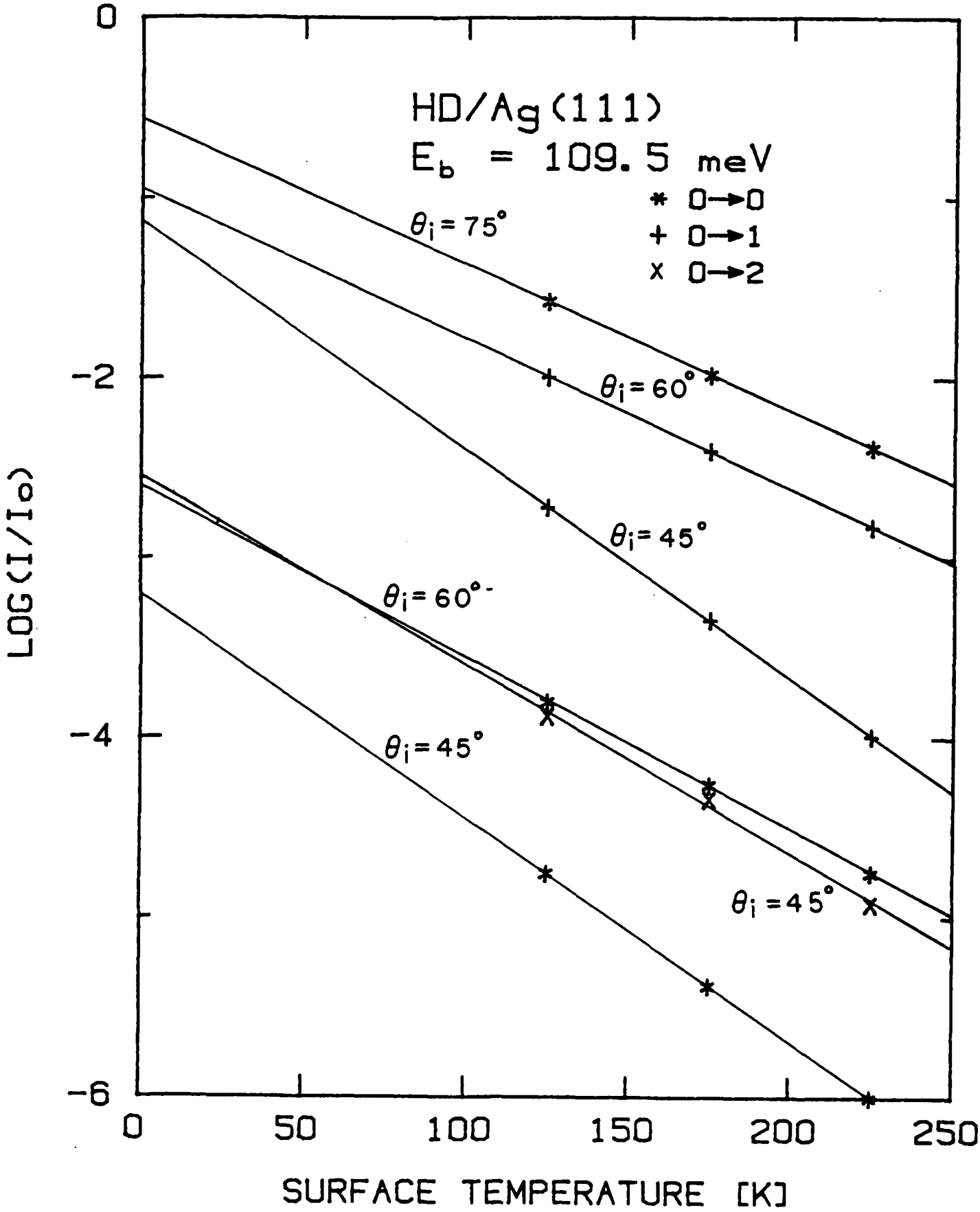
HD/Ag(111)
E_b = 109.5 meV
* 0→0
+ 0→1
x 0→2
θ_i = 75°
θ_i = 60°
θ_i = 45°
θ_i = 60°
θ_i = 45°
θ_i = 45°
LOG(I/Io)
0
-2
-4
-6
0
50
100
150
200
250
SURFACE TEMPERATURE [K]

FIGURE 7

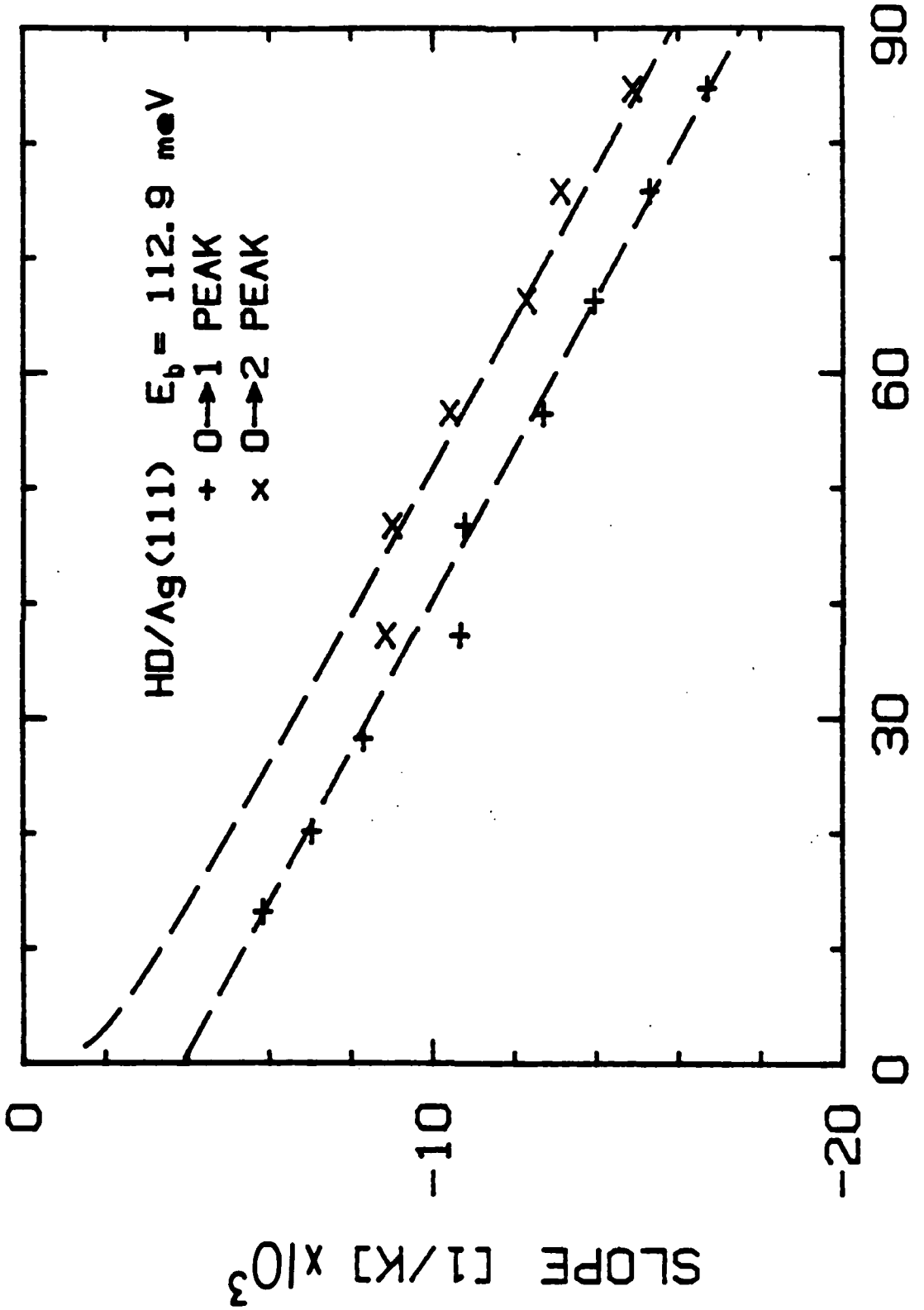
HD/Ag(111) E_b = 112.9 meV
+ 0→1 PEAK
x 0→2 PEAK
SLOPE [1/K] x10³
0
-10
-20
0
30
60
90
E_z [meV]

FIGURE 8

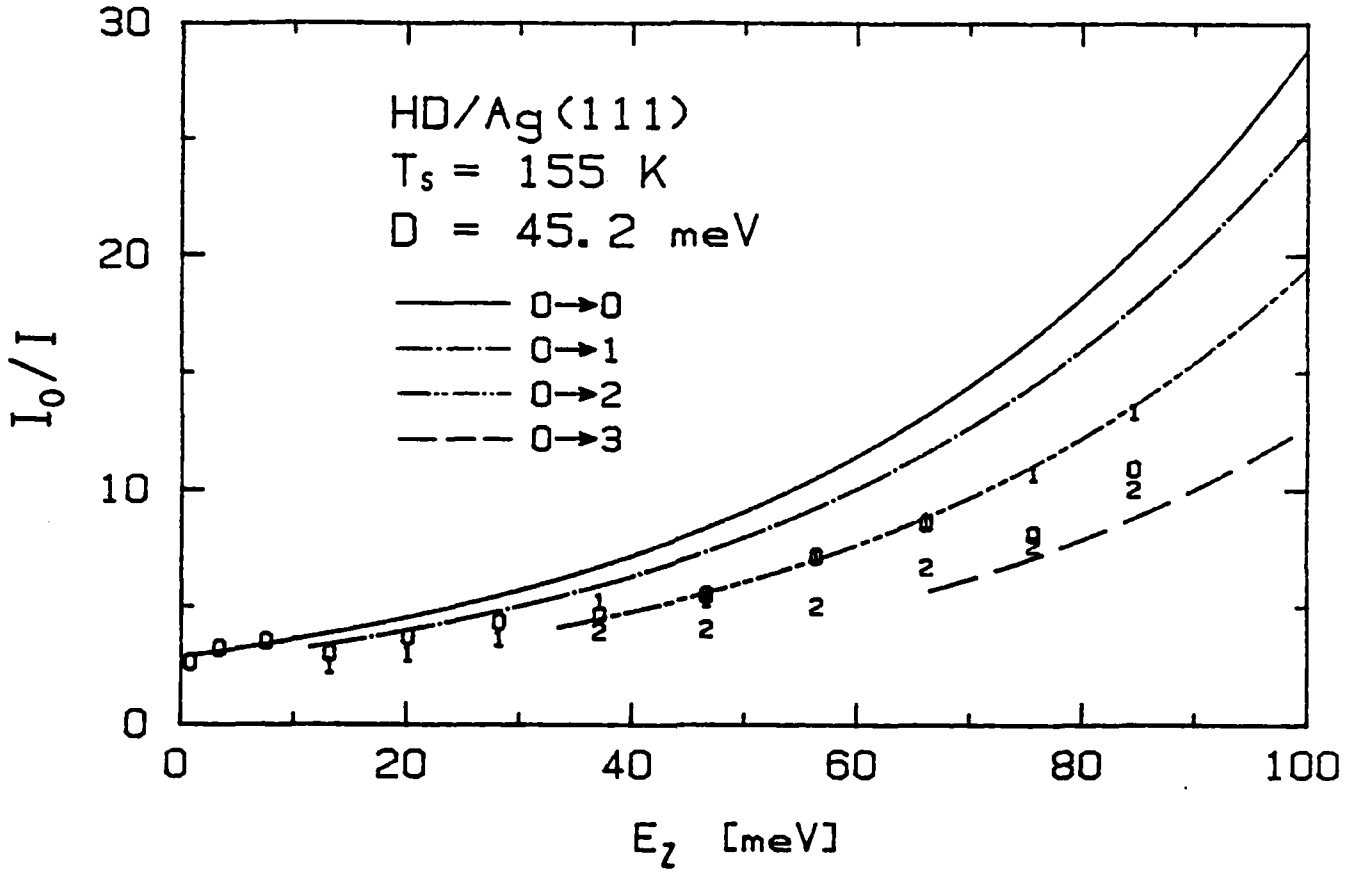
HD/Ag(111)
Ts = 155 K
D = 45.2 meV
0→0
0→1
0→2
0→3
I0/I
Ez [meV]
0
10
20
30
0
20
40
60
80
100

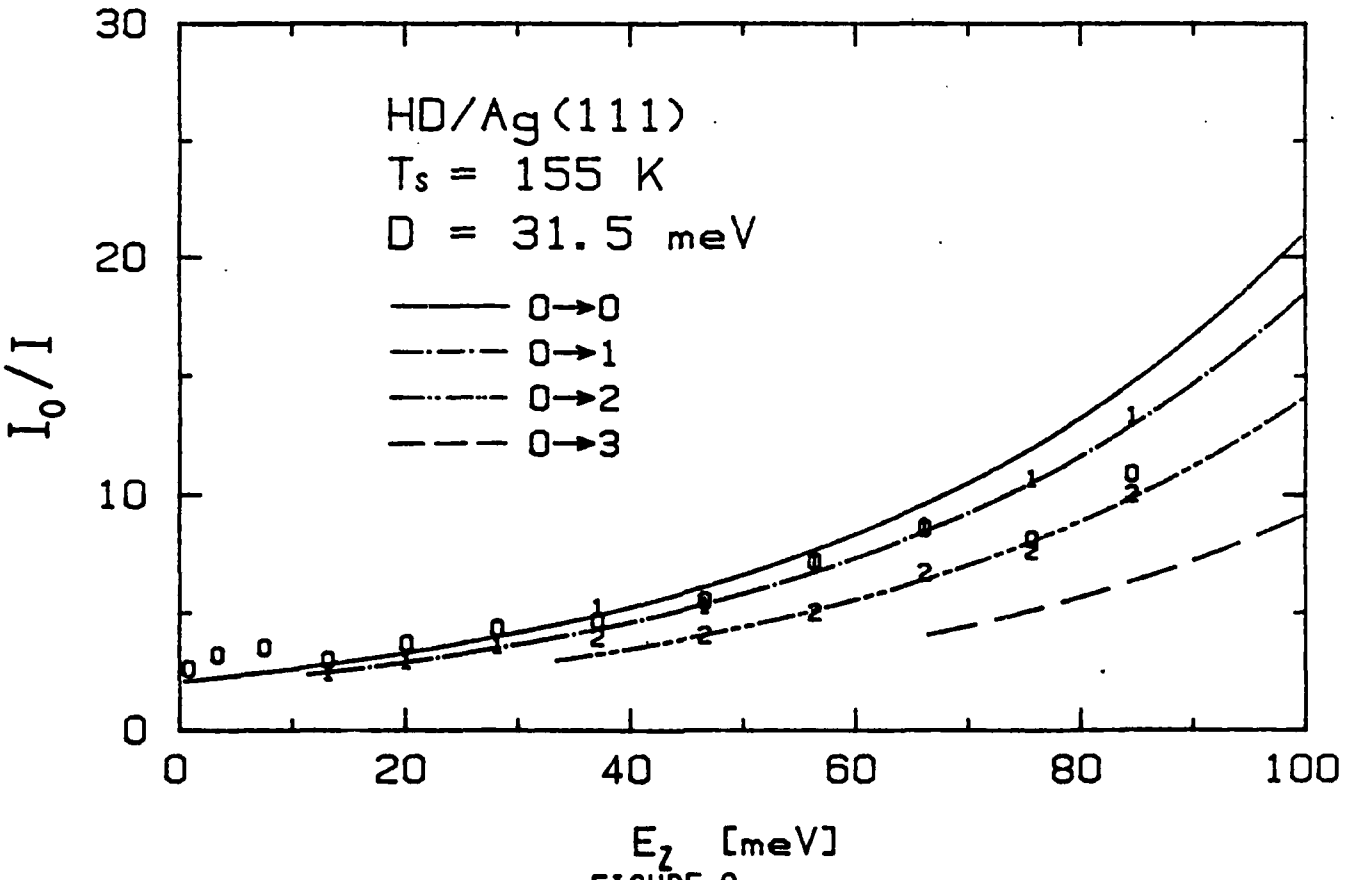
HD/Ag(111)
Ts = 155 K
D = 31.5 meV
0→0
0→1
0→2
0→3
I0/I
Ez [meV]
0
10
20
30
0
20
40
60
80
100

FIGURE 9

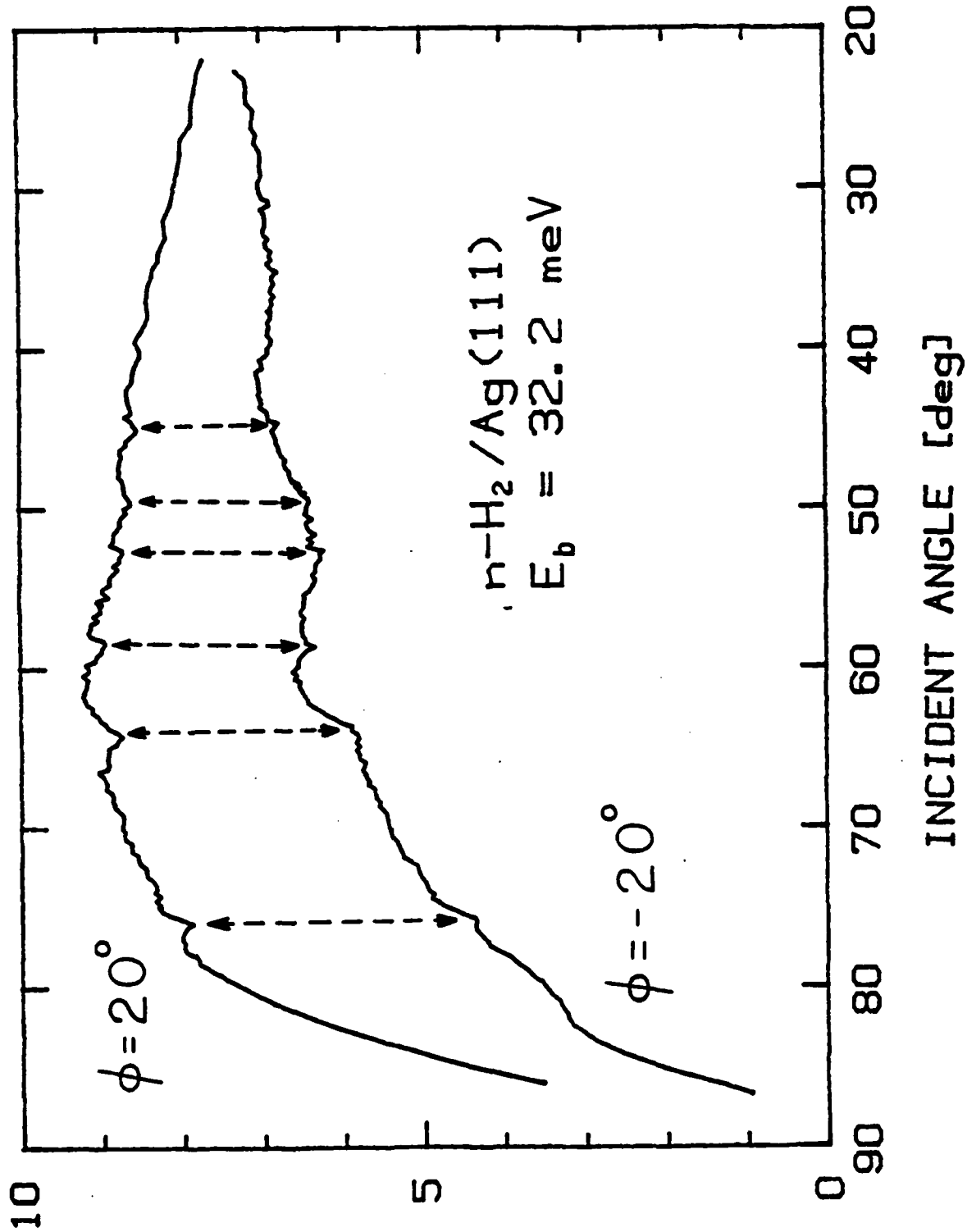
n-H2/Ag(111)
Eb = 32.2 meV
φ=20°
φ=-20°
SPECULAR INTENSITY (ARB. UNITS)
INCIDENT ANGLE [deg]
10
5
0
20
30
40
50
60
70
80
90

FIGURE 10

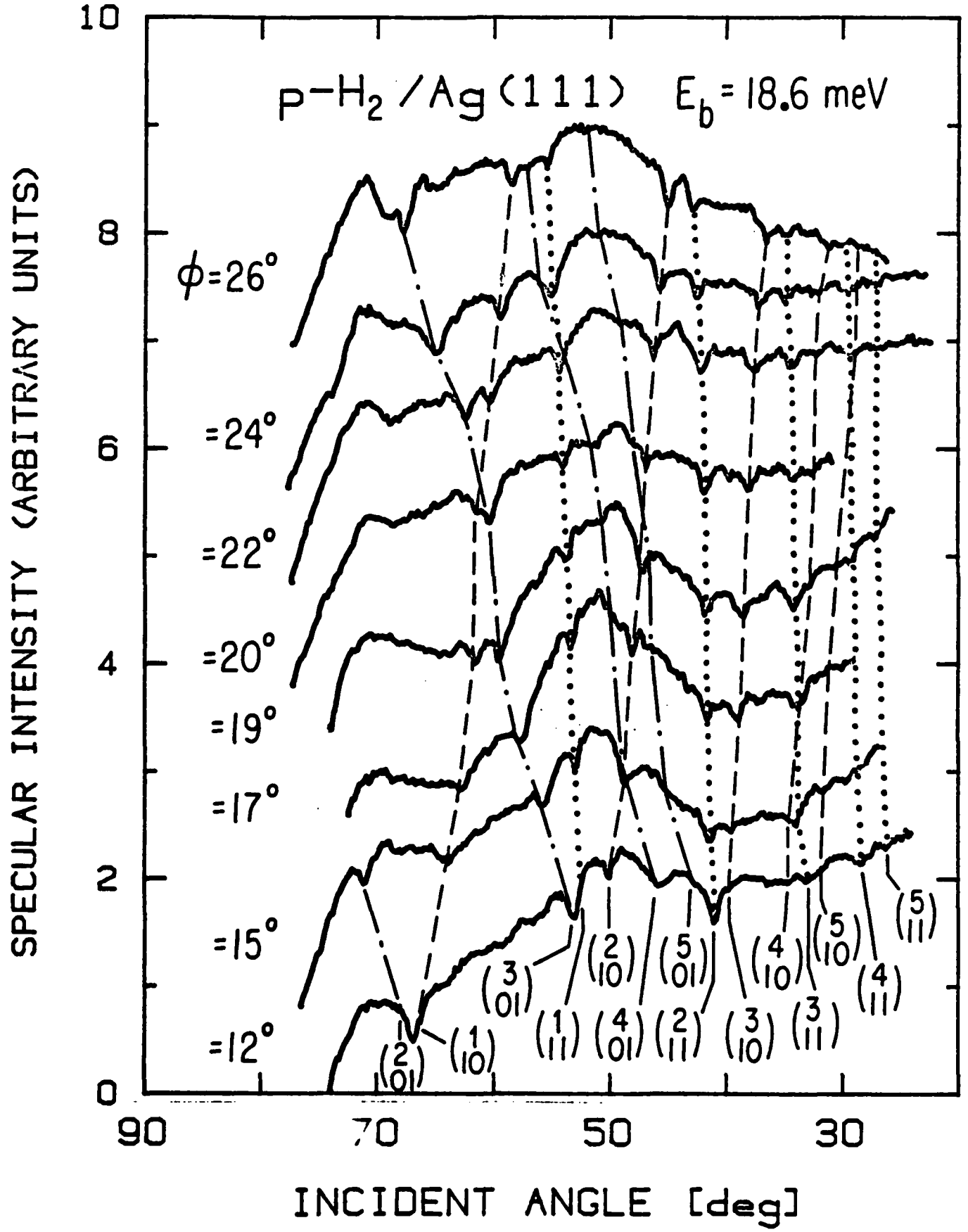
p-H2 / Ag(111) Eb = 18.6 meV
SPECULAR INTENSITY (ARBITRARY UNITS)
INCIDENT ANGLE [deg]
φ=26°
=24°
=22°
=20°
=19°
=17°
=15°
=12°
10
8
6
4
2
0
90
70
50
30
(2 0 1)
(1 1 0)
(3 0 1)
(1 1 1)
(2 1 0)
(4 0 1)
(5 0 1)
(2 1 1)
(4 1 0)
(3 1 0)
(5 1 0)
(3 1 1)
(4 1 1)
(5 1 1)

FIGURE 11

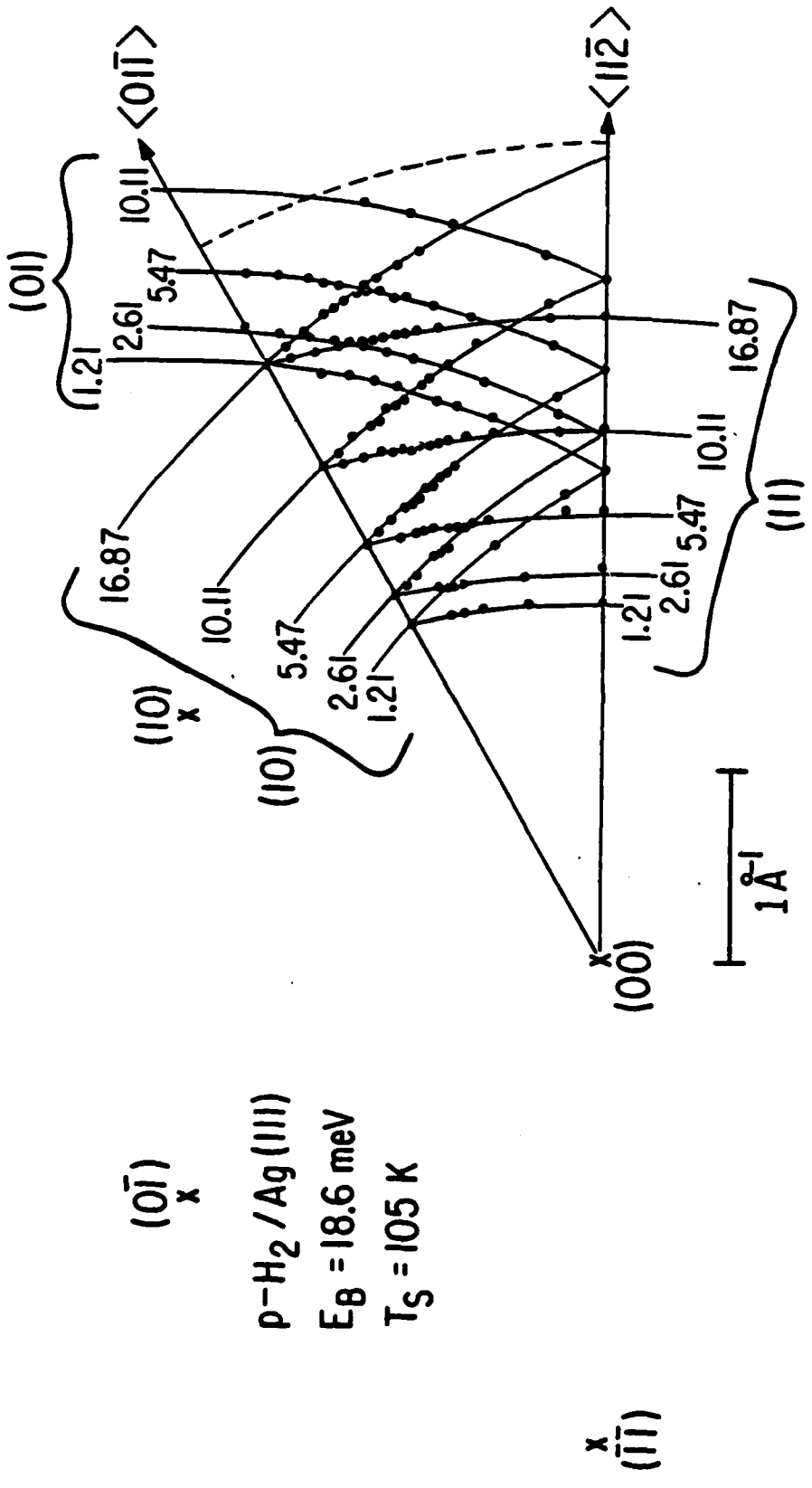
(01)
10.11
<011̄>
5.47
2.61
1.21
16.87
10.11
5.47
2.61
1.21
(10)
(10)
(01̄)
p-H2 / Ag (111)
EB = 18.6 meV
TS = 105 K
(11̄)
<112̄>
16.87
10.11
5.47
2.61
1.21
(11)
1 Å-1
(00)
(01)
(1̄0)

FIGURE 12

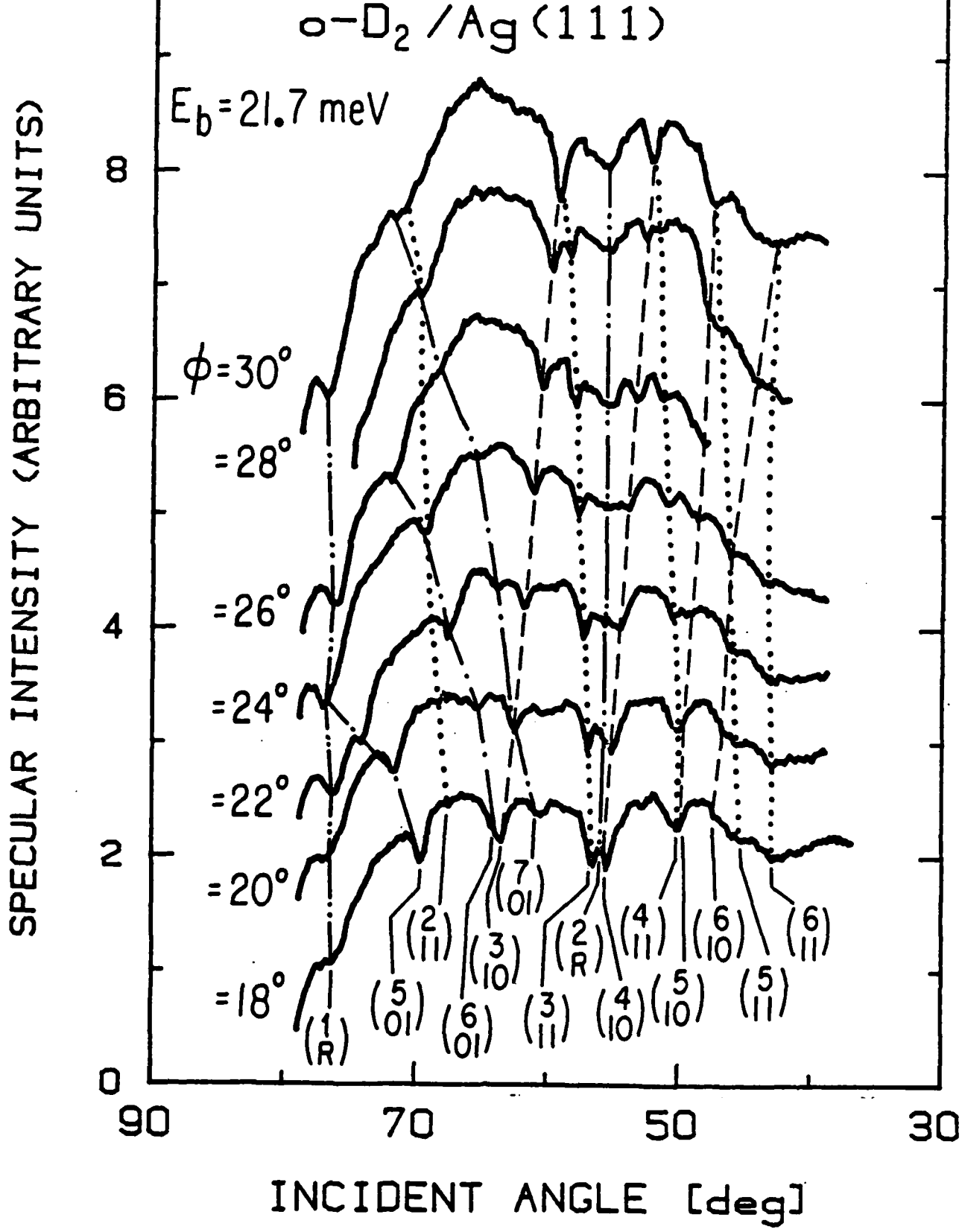
o-D2 /Ag(111)
Eb=21.7 meV
φ=30°
=28°
=26°
=24°
=22°
=20°
=18°
SPECULAR INTENSITY (ARBITRARY UNITS)
INCIDENT ANGLE [deg]
0
2
4
6
8
10
90
70
50
30
(1 R)
(5 01)
(6 01)
(2 11)
(3 10)
(7 01)
(3 11)
(2 R)
(4 10)
(4 11)
(5 10)
(6 10)
(5 11)
(6 11)

FIGURE 13

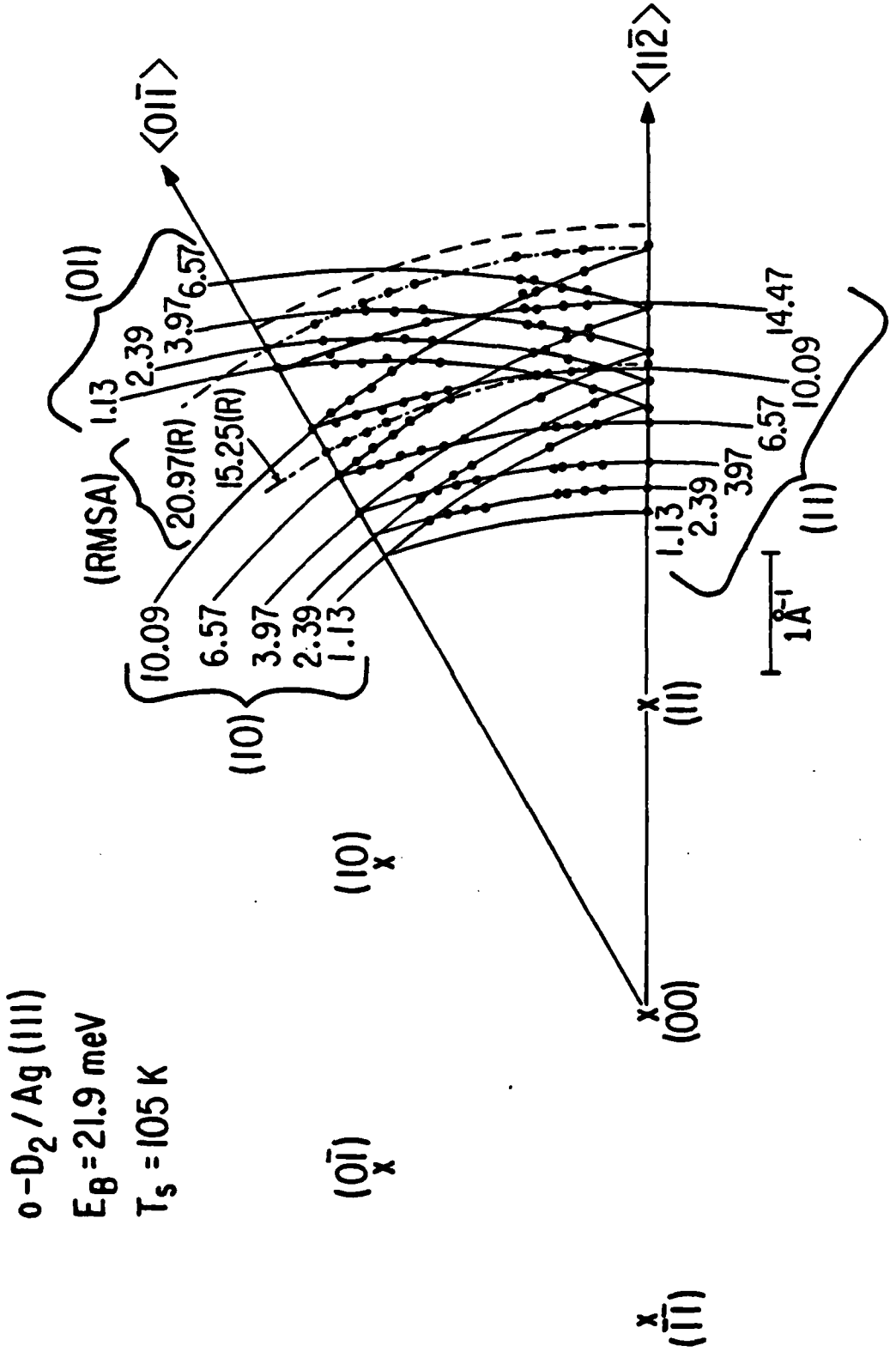
o-D2 / Ag (111)
EB = 21.9 meV
Ts = 105 K
(00)
(11)
(10)
(01)
(11)
(10)
(01)
(11)
(112)
(011)
(RMSA)
(011)
(111)
(110)
1.13
2.39
3.97
6.57
10.09
14.47
20.97(R)
15.25(R)
1Å-1

FIGURE 14

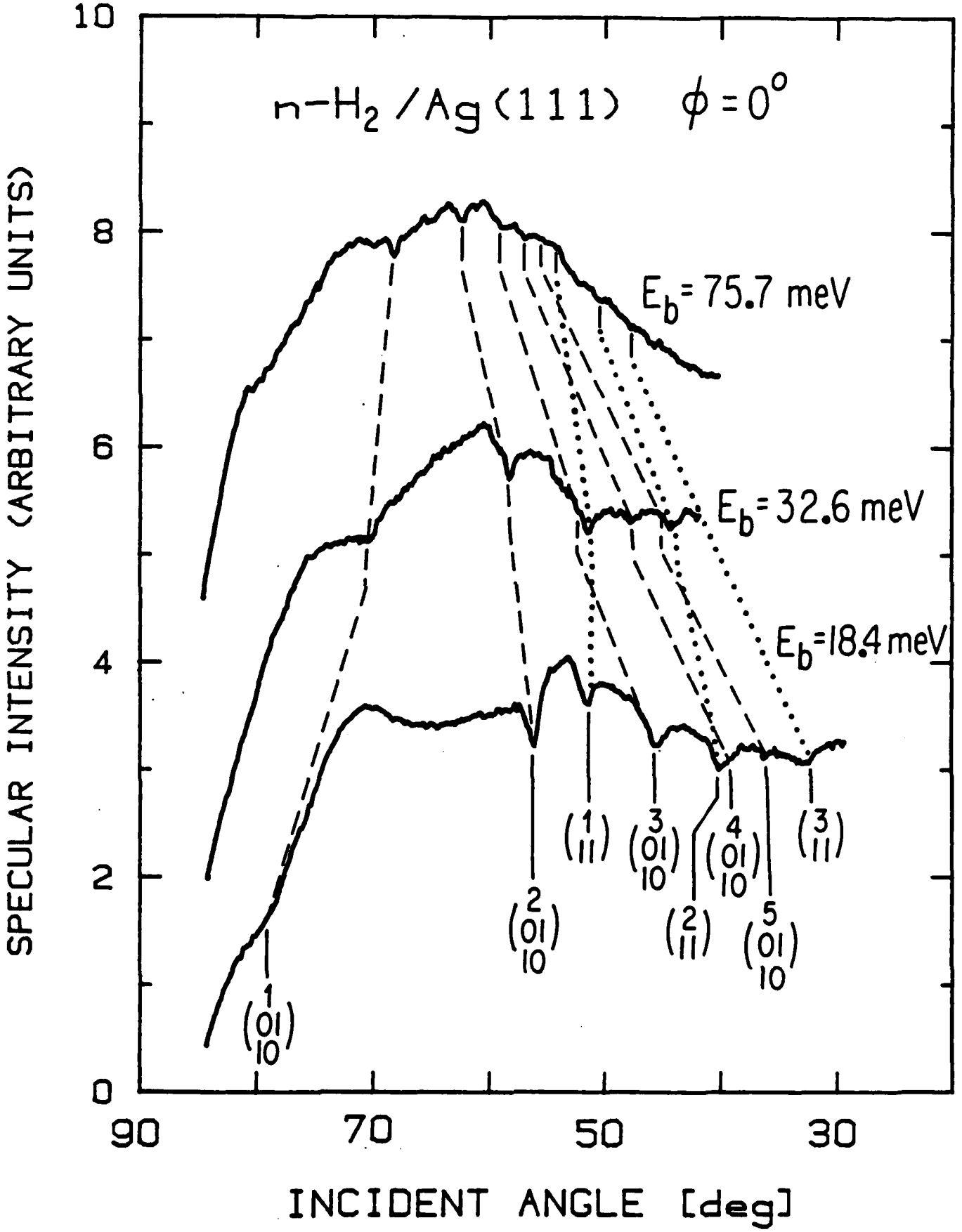
n-H2 /Ag(111) φ = 0°
Eb = 75.7 meV
Eb = 32.6 meV
Eb = 18.4 meV
(1 0 1 / 1 0)
(2 0 1 / 1 0)
(1 1 1)
(3 0 1 / 1 0)
(2 1 1)
(4 0 1 / 1 0)
(5 0 1 / 1 0)
(3 1 1)
SPECULAR INTENSITY (ARBITRARY UNITS)
INCIDENT ANGLE [deg]
0
2
4
6
8
10
90
70
50
30

FIGURE 15

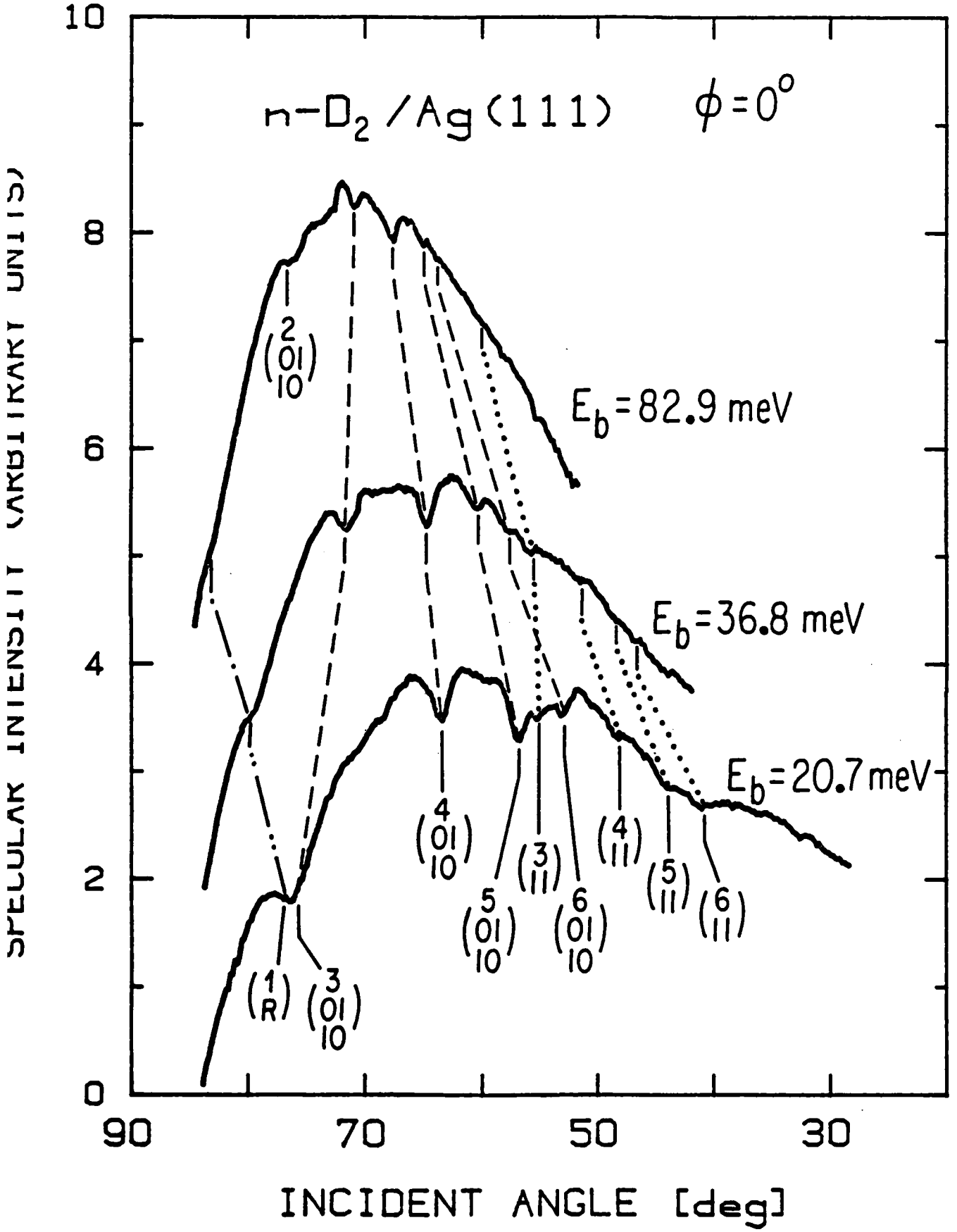
n-D2 /Ag(111) φ=0°
Eb=82.9 meV
Eb=36.8 meV
Eb=20.7 meV
(2 0 1 10)
(1 R)
(3 0 1 10)
(4 0 1 10)
(5 0 1 10)
(3 1 1)
(6 0 1 10)
(4 1 1)
(5 1 1)
(6 1 1)
SPECULAR INTENSITY (ARBITRARY UNITS)
INCIDENT ANGLE [deg]
0
2
4
6
8
10
90
70
50
30

FIGURE 16

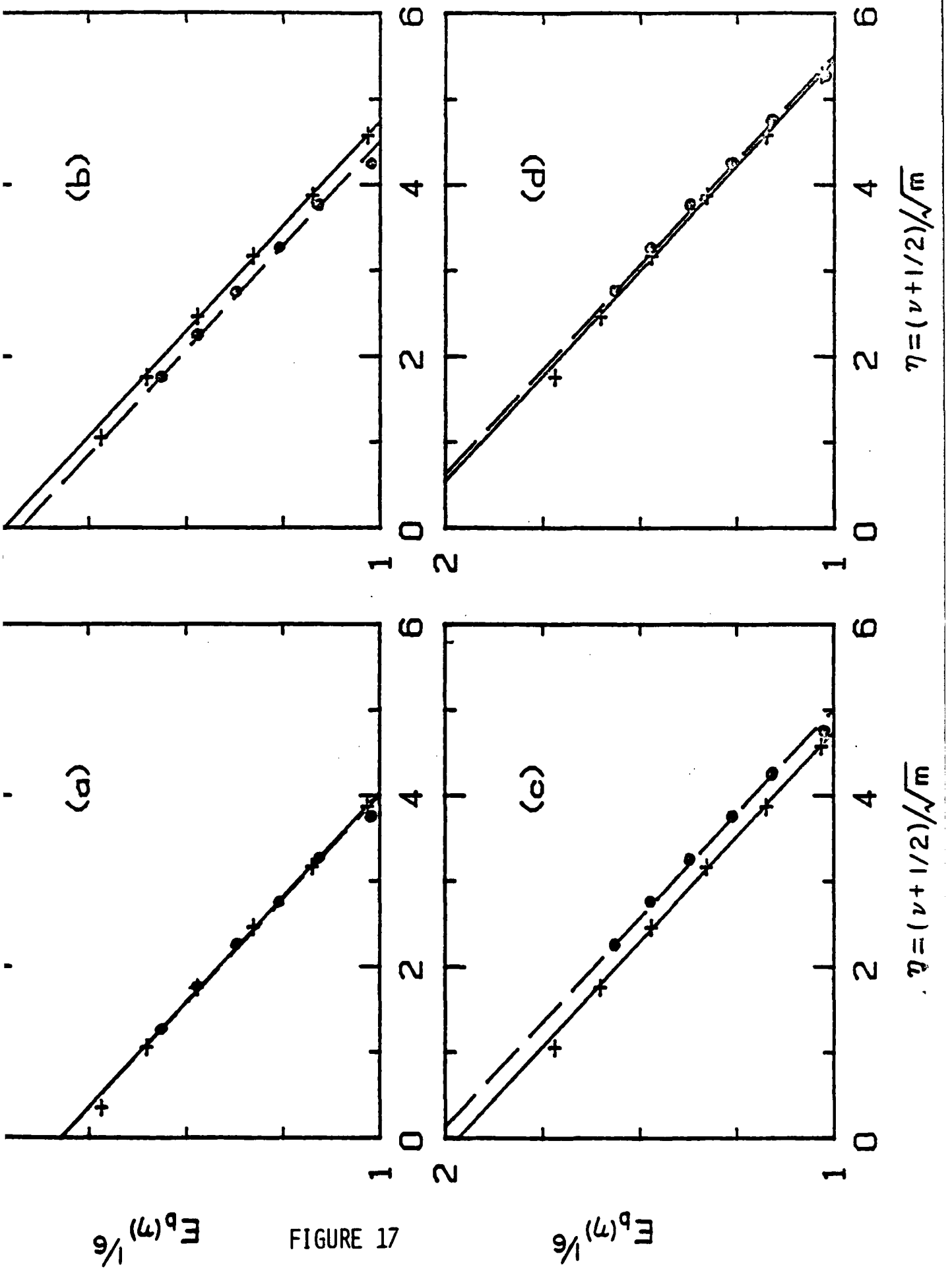

FIGURE 17

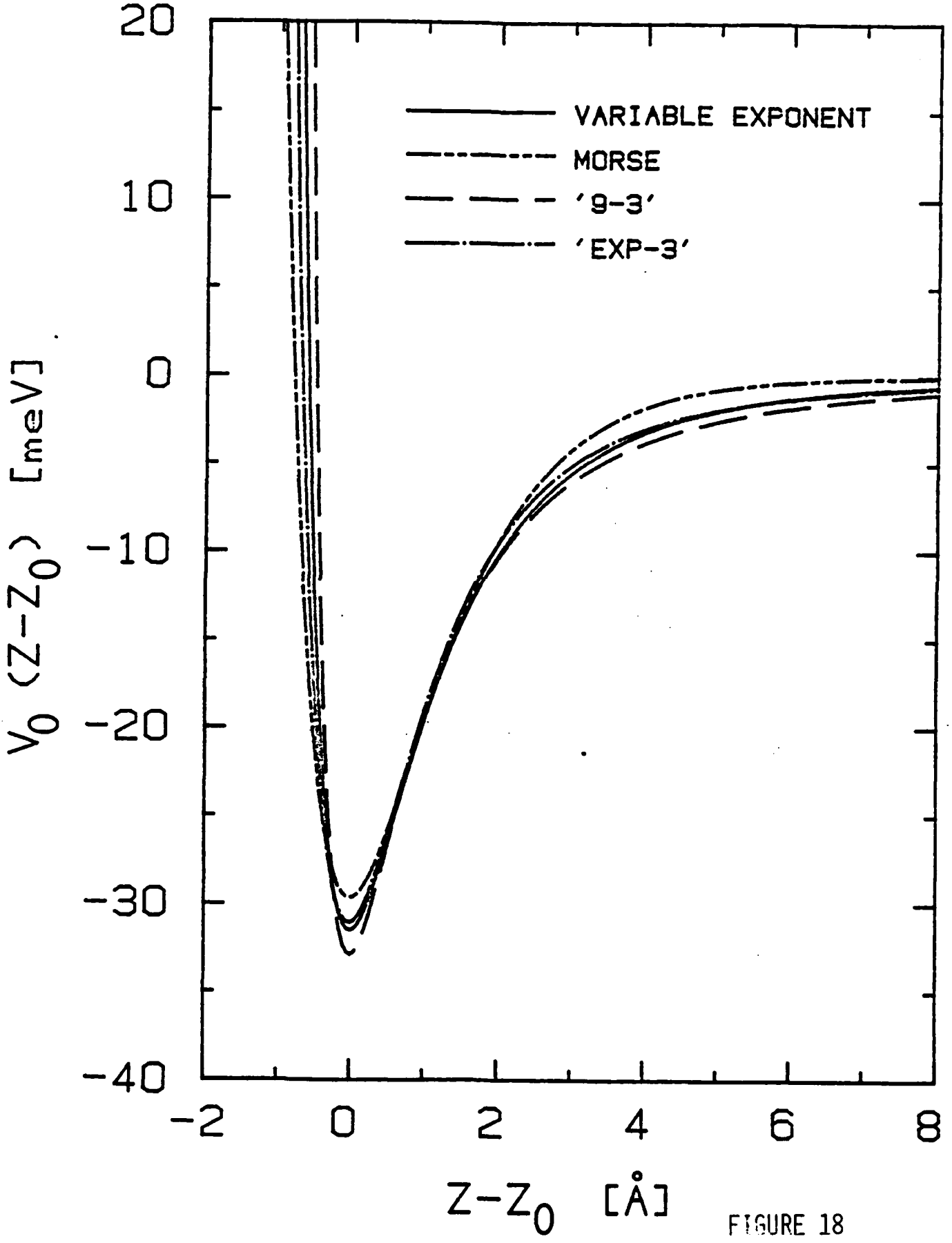
VARIABLE EXPONENT
MORSE
'9-3'
'EXP-3'
20
10
0
-10
-20
-30
-40
-2
0
2
4
6
8
$V_0\,(Z-Z_0)$ [meV]
$Z-Z_0$ [Å]

FIGURE 18

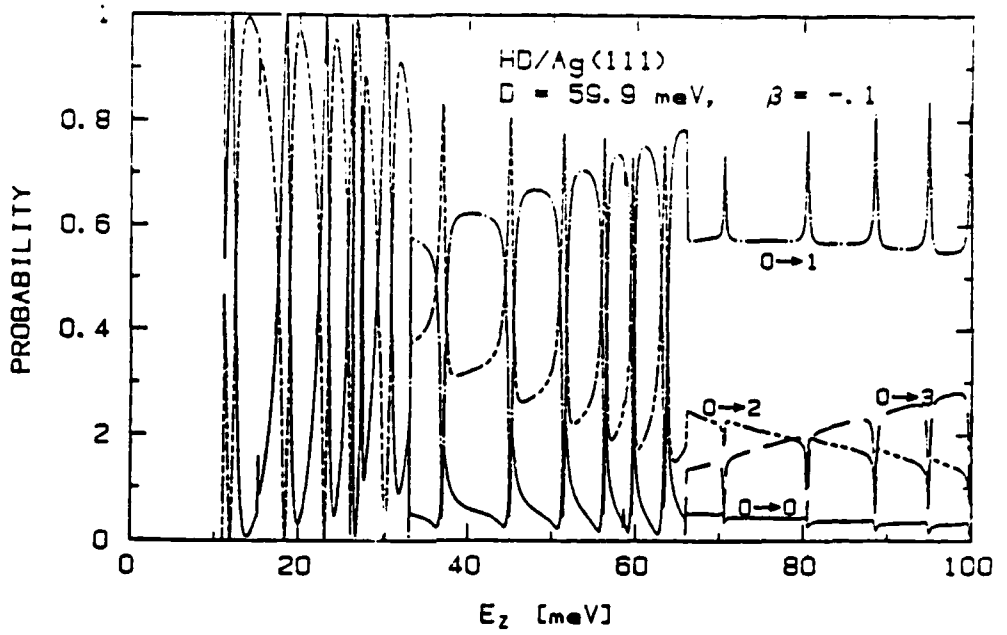
HD/Ag(111)
D = 59.9 meV, β = -.1
PROBABILITY
0→1
0→2
0→3
0→0
0
0.2
0.4
0.6
0.8
0
20
40
60
80
100
E_z [meV]

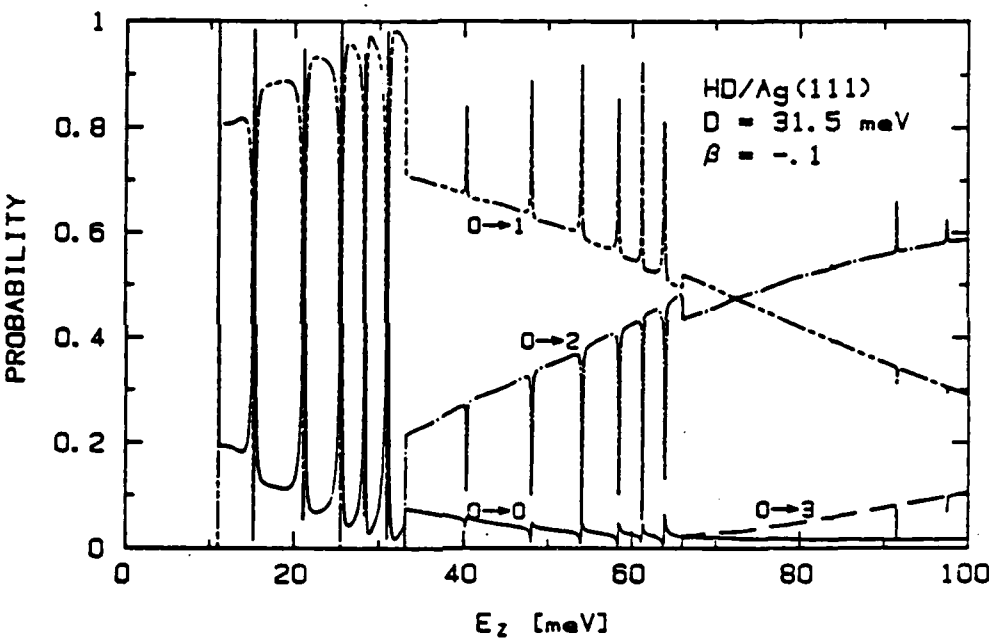
HD/Ag(111)
D = 31.5 meV
β = -.1
PROBABILITY
0→1
0→2
0→0
0→3
0
0.2
0.4
0.6
0.8
1
0
20
40
60
80
100
E_z [meV]

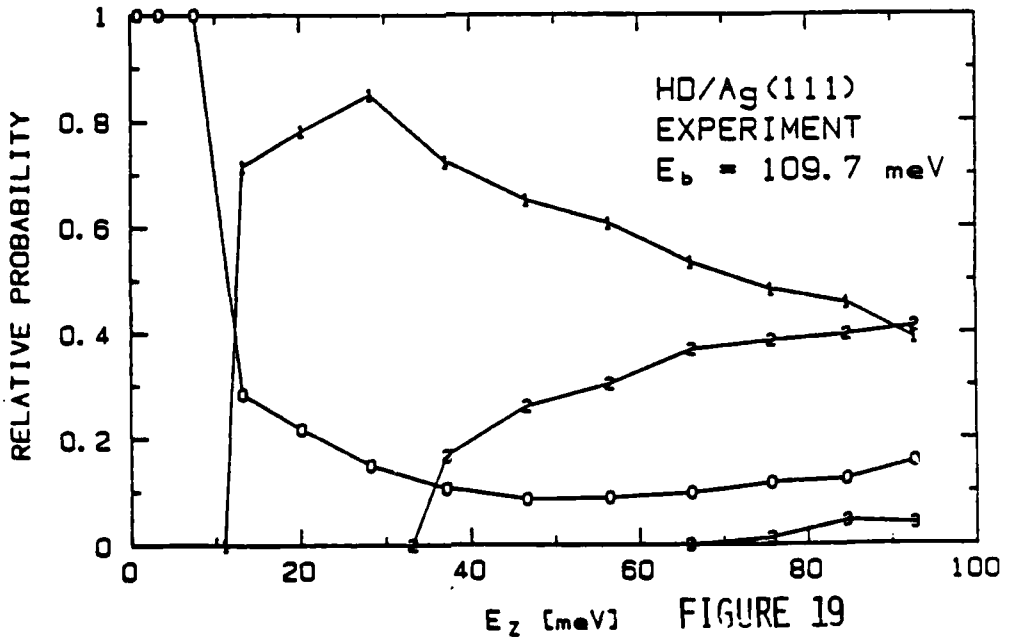
HD/Ag(111)
EXPERIMENT
E_b = 109.7 meV
RELATIVE PROBABILITY
0
0.2
0.4
0.6
0.8
1
0
20
40
60
80
100
E_z [meV]

FIGURE 19

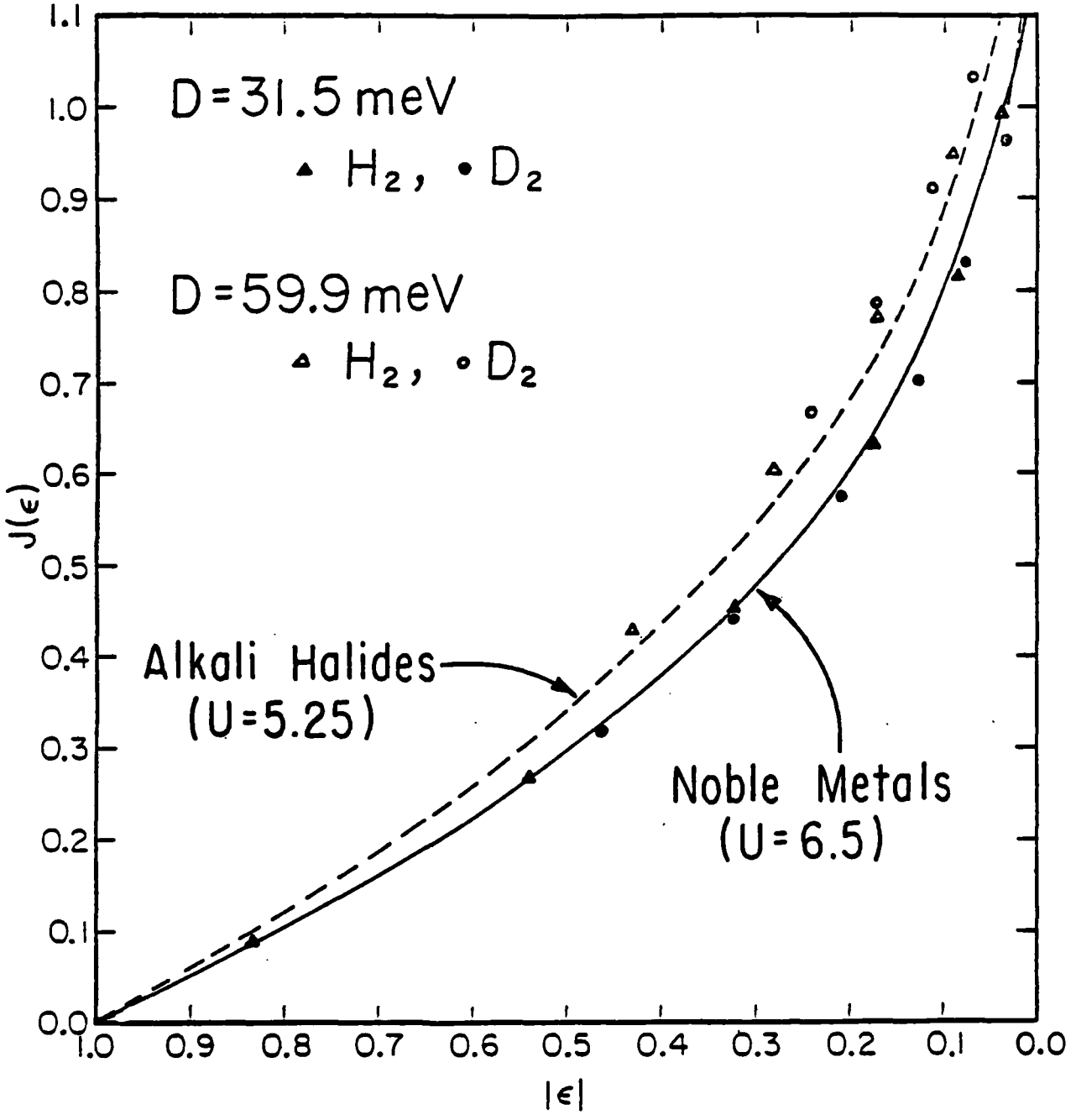
D=31.5 meV
▲ H2, • D2
D=59.9 meV
△ H2, ○ D2
Alkali Halides
(U=5.25)
Noble Metals
(U=6.5)
J(ε)
|ε|
1.1
1.0
0.9
0.8
0.7
0.6
0.5
0.4
0.3
0.2
0.1
0.0
1.0 0.9 0.8 0.7 0.6 0.5 0.4 0.3 0.2 0.1 0.0

FIGURE 20

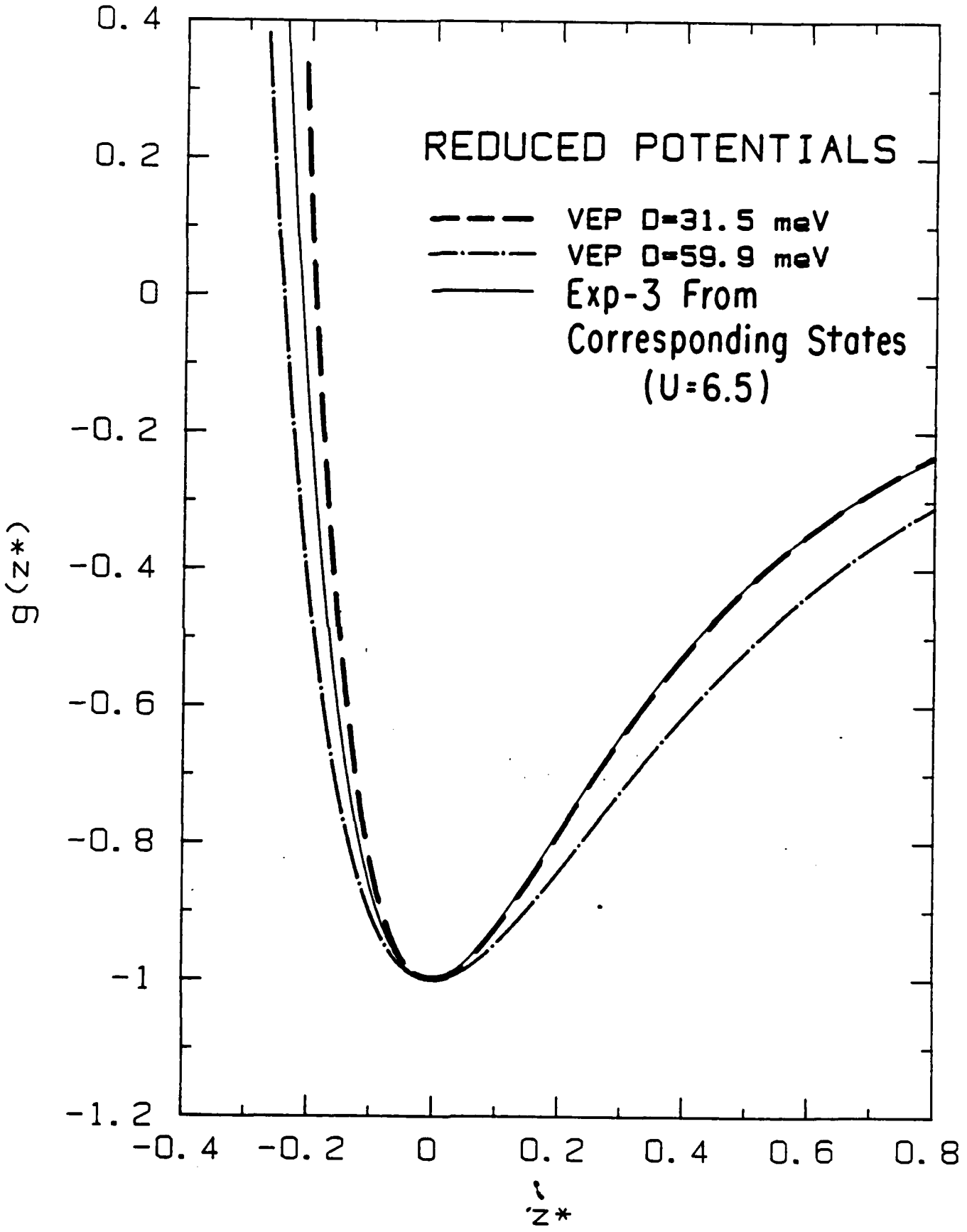
REDUCED POTENTIALS
VEP D=31.5 meV
VEP D=59.9 meV
Exp-3 From
Corresponding States
(U=6.5)
g(z*)
z*
0.4
0.2
0
-0.2
-0.4
-0.6
-0.8
-1
-1.2
-0.4
-0.2
0
0.2
0.4
0.6
0.8

FIGURE 21

END

FILMED

11-85

DTIC